ACSNANO

www.acsnano.org

ARTICLE

Many Birds, One Stone: A Smart Nanodevice for Ratiometric Dual-Spectrum Assay of Intracellular MicroRNA and Multimodal Synergetic Cancer Therapy

Peng He, Wenhao Han, Cheng Bi, Weiling Song, Shuyan Niu, Hong Zhou, and Xiaoru Zhang*

Cite This: *ACS Nano* 2021, 15, 6961−6976

Read Online

ACCESS | Metrics & More | Article Recommendations | Supporting Information

ABSTRACT: The development of a theragnostic platform integrating precise diagnosis and effective treatment is significant but still extremely challenging. Herein, an integrated smart nanodevice composed of Au@$Cu_{2-x}S$@polydopamine nanoparticles (ACSPs) and fuel DNA-conjugated tetrahedral DNA nanostructures (fTDNs) was constructed, in which the ACSP nanoprobe played multiple key roles in antitumor therapy as well as *in situ* monitoring of microRNAs (miRNAs) in cancer cells. Regarding the analysis, the ACSP probe contained two optical properties: excellent surface-enhanced Raman scattering (SERS) enhancement and high fluorescence (FL) quenching performance. Employing the ACSPs as the high-efficiency detection substrate combined with the fTDN-assisted DNA walking nanomachines as the superior amplification strategy, a SERS-FL dual-spectrum biosensor was constructed, which achieved an ultralow background signal and excellent sensitivity with detection limits of 0.11 pM and 4.95 aM by FL and SERS, respectively. Moreover, the rapid FL imaging and precise SERS quantitative detection for miRNA in cancer cells were also achieved by dual-signal ratio strategy, improving the accuracy of diagnosis. Regarding the therapeutic application, due to the high reactive oxygen species generation ability and excellent photothermal conversion efficiency, the ACSPs can also act as an all-in-one nanoagent for multimodal collaborative tumor therapy. Significantly, both *in vivo* and *in vitro* experiments confirmed its high biological safety and strong anticancer effect, indicating its promising theragnostic applications.

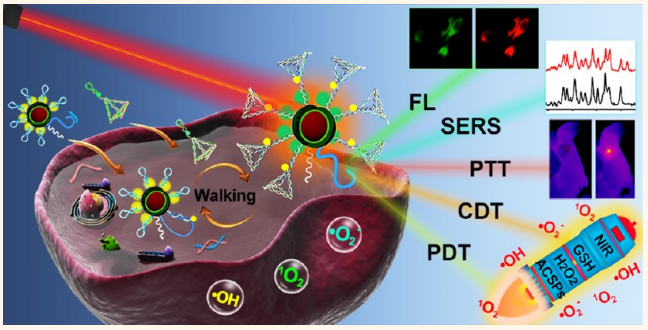

KEYWORDS: *dual-spectrum assay, DNA walking nanomachine, in situ imaging, all-in-one nanoagent, synergetic therapy*

At present, cancer is one of the most serious threats to human health, and the number of cancer cases is still increasing.[1] Accurate diagnosis and efficient therapy of tumors at their earliest stages are of great significance to improve the cure rate of tumors.[2,3] MicroRNA (miRNA), as a promising biomarker, plays an important role in the regulation of tumor-associated genes.[4−7] Its aberrant expression might provide valuable information for the occurrence and progression of multiple cancers.[8,9] Therefore, the reliable analysis of miRNA is crucial for clinical diagnosis, targeted therapy, and prognosis monitoring. *In situ* bioimaging and detection of miRNAs in single living cells have been increasingly used to elucidate the spatiotemporal distribution information on miRNAs and monitor tumor treatment progress.[10−12] However, there are still serious challenges to accurately detect intracellular miRNA due to the complex tumor environment and the extremely low abundance of miRNAs in tumor cells. In recent years, surface-enhanced Raman scattering (SERS) has received great attention due to its advantages of high sensitivity, "fingerprint" signatures, low phototoxicity, resistance to photobleaching, and *in situ* detection.[13−15] Particularly, there is low autofluorescence in the red to near-infrared region of the electromagnetic spectrum and high signal enhancement based on the localized surface plasmon resonance (LSPR) effects of noble metal nanomaterial, which make SERS an appealing diagnostic tool for

Received: December 27, 2020
Accepted: March 29, 2021
Published: April 6, 2021

https://doi.org/10.1021/acsnano.0c10844
ACS Nano 2021, 15, 6961−6976

Scheme 1. Schematic of Ratiometric Dual-Spectrum Assay of MicroRNA and Multimodal Collaborative Tumor Therapy[a]

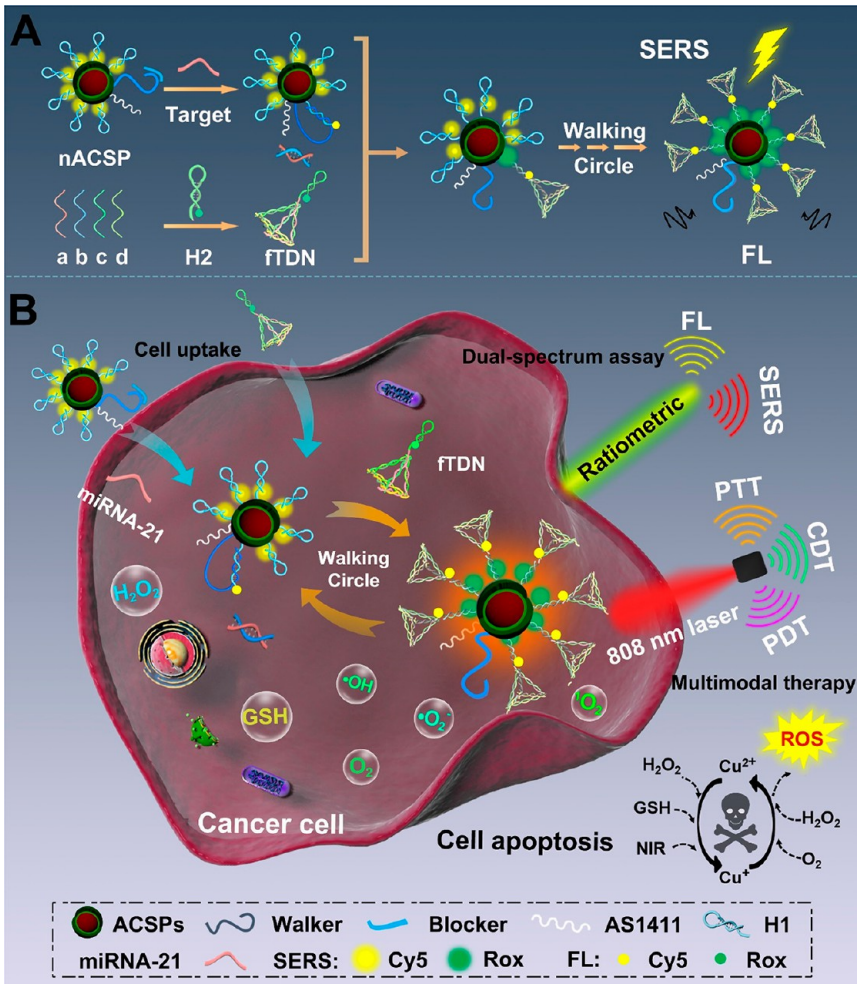

[a](A) Design of the fTDN-assisted DNA walking nanomachine for simultaneous ratiometric SERS-FL assay of miRNA-21. (B) Illustration of the developed nanodevice for miRNA detection and imaging in live cells and ACSPs-mediated multimodal synergistic therapy.

biological analysis in live cells.[16−19] Nevertheless, SERS imaging analysis at the single-cell level still has some limitations, such as low imaging speed, dependency on an enhancement substrate, and complex biological background interference, which seriously restrict the further application of the SERS technique. Fortunately, compared with SERS, fluorescence-based assays could provide reciprocal signals and higher spatiotemporal resolution, despite their low sensitivity.[20] Alternatively, ratiometric measurements are capable of self-calibration by recording the ratio change of two measurable signal intensities, effectively mitigating environmental interference and false positive signals.[21−23] Thus, the combination of the ratiometric strategy and SERS-fluorescence double spectra imaging technology could achieve faster positioning, more precise detection, and more diagnostic information by integrating the advantages of different single modes. This sensing platform could be a trend-setting analysis technique. Ye *et al.* developed a seesaw ratiometric probe for the sensitive detection of telomerase activity in a single living cell using a dual-spectrum.[24] However, in many cases, the amount of miRNA in the tumor cells was below the detection threshold of effectively triggering the sensing probe. It is highly imperative to develop a powerful intracellular signal amplification method for the dynamic monitoring of miRNA.

Dynamic DNA nanomachines could implement biological computing, transmission signals, and particular mechanical operations based on Strict Watson−Crick base pairing rules. The high specificity and programmability of hybridization make DNA nanodevices a compelling tool for signal amplification and logical assembly. A variety of DNA nanomachines, such as DNA tweezers,[25] DNA robots,[26] molecular motors,[27] and DNA walkers,[28−30] have been constructed and applied to biological analysis. Among these nanomachines, the DNA walker, as an attractive signal enhancement circuit, has received great attention. Activated by a target molecule, the DNA walker can automatically move along a predesigned track driven by DNAzymes, nicking endonuclease, and strand displacement.[28] Signal amplification and functional biological operation are achieved with alternating responses and reversible interactions. In particular, the three-dimensional (3D) walking nanomachines assembled into external nanoparticles are favorable in terms of signal enhancement due to the greater mobility and load capacity. These nanomachines have been further adapted in the biosensing and imaging of low-abundance biomolecules.[29,30] However, to the best of our knowledge, the combination of a 3D DNA walker with the ratiometric SERS-fluorescence dual

https://doi.org/10.1021/acsnano.0c10844
ACS Nano 2021, 15, 6961−6976

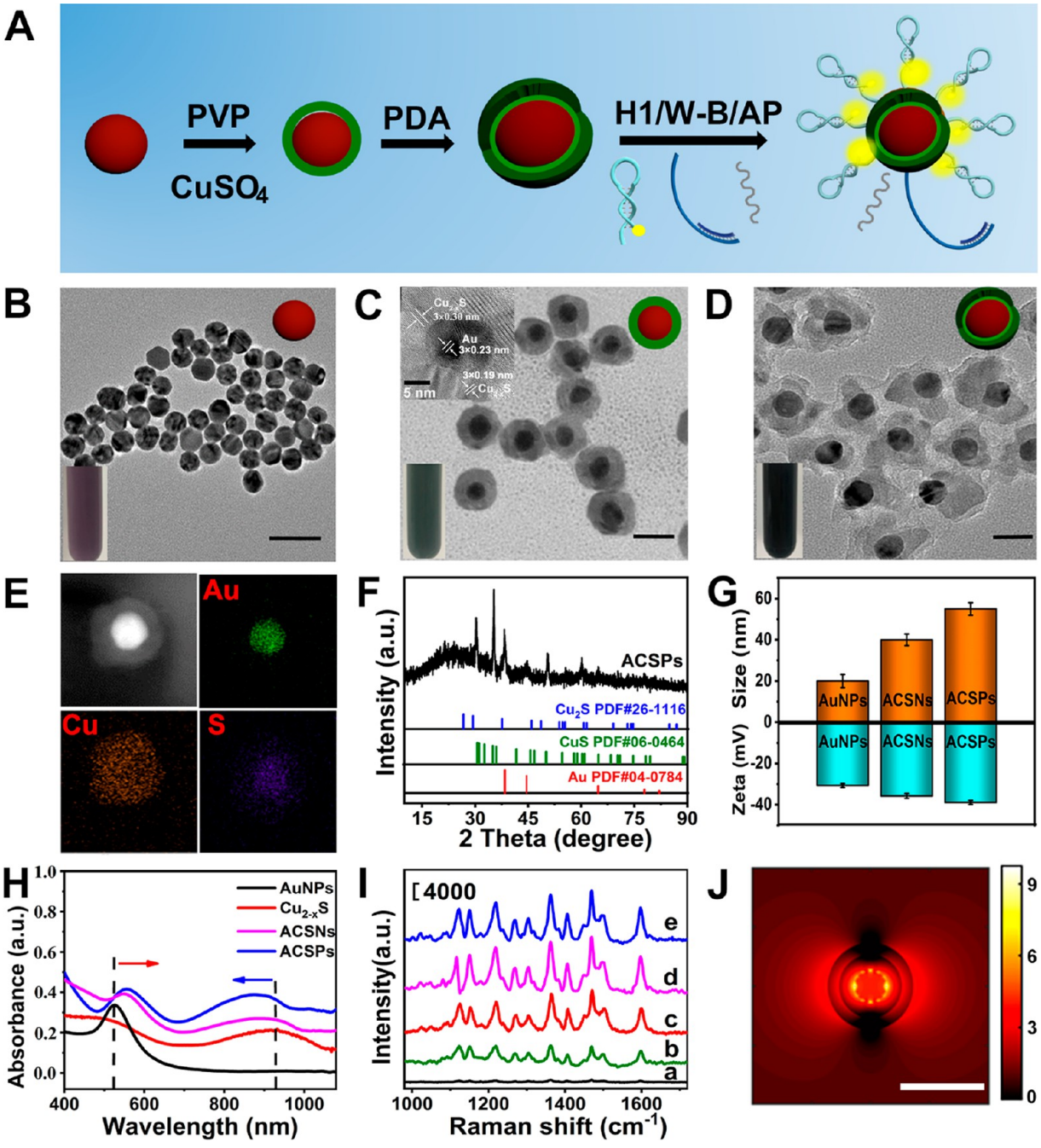

Figure 1. Synthesis and characterization of nACSPs. (A) Illustration of the nACSPs synthetic process. TEM images of AuNPs (B), ACSNs (C, inset shows the HRTEM images of ACSNs) and ACSPs (D). Scale bar: 50 nm. (E) Elemental mapping of Au, Cu, S of ACSNs. (F) XRD patterns of ACSPs (the standard lines of Au, CuS and Cu_2S are supplied for comparison). (G) The ζ potential and hydrodynamic diameter of ACSPs. (H) UV−vis-NIR spectra of AuNPs (a), $Cu_{2-x}S$ (b), ACSNs (c), and ACSPs (d). (I) Raman spectra of Cy5 (a), AuNPs-H1 (b), ACSNs-H1 (c), ACSPs-H1 (d), and ACSPs-H1 after 7 days (e), respectively (excited with a 633 nm laser). (J) Electromagnetic field distribution of ACSPs obtained by FDTD simulation at 633 nm. Scale bar: 50 nm.

mode platform for the sensitive detection and imaging of miRNAs in living cells has not been reported.

A theragnostic platform integrating diagnostic and therapeutic functions has been the focus of current research. The main therapies include surgery,[31] chemotherapy, radiotherapy (RT), photothermal therapy (PTT),[32] gene therapy (GT),[33] and reactive oxygen species (ROS)-mediated oncotherapy.[34−36] Among these therapies, PTT and ROS-mediated treatment have attracted widespread attention due to their non-invasive nature, deep penetration, high efficiency, and few side effects.[37] Plasmonic copper sulfide with numerous copper deficiencies ($Cu_{2-x}S$) has attracted wide attention because of its NIR-induced photothermal properties and its ability to generate sufficient ROS in biological media.[38−40] In addition, Au@$Cu_{2-x}S$ dual plasmonic nanoprobes possess SERS and photothermal enhanced effects due to localized surface plasmon resonance (LSPR) coupling.[41,42] However, the addition of stabilizers during the material preparation process makes these nanoprobes difficult to postmodify and functionalize, limiting diagnostic application. Moreover, due to the low

https://doi.org/10.1021/acsnano.0c10844
ACS Nano 2021, 15, 6961−6976

redox potential of Cu^{2+}/Cu^{+}, the free copper ions generated by the $Cu_{2-x}S$-based nanosystem in the circulation may cause damage to healthy tissues.[43−45] Therefore, it is still a significant challenge to develop an all-in-one nanosystem with multimodal imaging and synergistic therapeutic effects for simultaneous precision monitoring and cancer treatment. Herein, we fabricated an integrated smart nanodevice for accurate diagnosis of intracellular miRNA and synergetic therapy of tumor cells, in which Au@$Cu_{2-x}S$@polydopamine nanoparticles (ACSPs) played dual key roles in tumor therapy and *in situ* SERS-FL monitoring. On the one hand, an ultrasensitive ratiometric dual-spectrum assay platform based on tetrahedral DNA assistant walker amplification was employed to detect tumor-related miRNAs. The developed ACSP nanoprobe served as the dual-mode detection probe to achieve SERS enhancement and fluorescence quenching of the signal molecules. In this system, a smart 3D DNA walking nanomachine was delicately designed to improve the detection sensitivity. The dual-signal ratio determination with self-calibration capability was more stable, more accurate, and less susceptible to environmental interference than previous nanowalkers. The SERS-FL dual spectra assay provided comprehensive and intuitive information for microRNA analysis in living cells. On the other hand, ACSPs could also act as a multifunctional nanoagent when combined with PTT, photodynamic therapy (PDT), and chemodynamic therapy (CDT), realizing excellent synergistic tumor treatment. This versatile nanoplatform with a smart design exhibits considerable potential for clinical diagnosis and therapy.

RESULTS AND DISCUSSION

Principles of a Dual Ratiometric SERS-FL Biosensor Based on a 3D DNA Walking Nanomachine. As shown in Scheme 1A, the 3D DNA walking nanomachine contained nucleic acid-functionalized ACSPs (nACSPs) and a fuel DNA-conjugated tetrahedral DNA nanostructure (fTDN) with dual SERS and FL ratio signals. The nACSPs were assembled with 5′-thiolated and 3′-Cy5-labeled hairpin DNA (H1) as the track and 5′-thiolated AS1411 aptamer (AP) and 5′-thiolated walker DNA (W) as the walking leg that was partially hybridized with a special blocker DNA (B). The B has two interrelated effects: target recognition and background reduction. As the detection substrate, the ACSPs not only exhibited strong SERS enhancement but also had a high fluorescence quenching effect. The tetrahedral DNA nanostructure (TDN) was fabricated with four programmable DNA strands (TDNa−TDNd, Table S1). Among the four single-stranded DNAs, the sequence of TDNa was extended with a link sequence to hybridize with 3′-Rox-labeled hairpin DNA (H2), which acted as the walking fuel. TDNd contained another different extended sequence, the AS1411 aptamer. AS1411 can specifically recognize the overexpressed nucleolin ontumor cell surfaces, which would contribute to the directional accumulation of nanomachines at the tumor cell surfaces and improve their cellular uptake efficiency. MicroRNA-21 (miR-21) was selected as the model miRNA in our experiments. MiR-21 is recognized as an oncogene and is overexpressed by most cancer cells. In dual SERS and FL modes, the distance change between the ACSPs and the signal molecules could trigger reciprocal spectral signal conversion. Scheme 1B shows that the walker nanomachine was inactive in the absence of a target because the walking activity of W was blocked by B. H1 and H2 retained their stable hairpin structure, and the Cy5-tag on H1 was close to the ACSP surface when the Cy5 SERS signal was on and its fluorescence signal was off, while the Rox-tagged H2 on fTDN was not close to the ACSP probe when the Rox SERS signal was off and its fluorescence was on. In this state, only the strong SERS signal of Cy5 and the fluorescence signal of Rox could be detected. However, in the presence of target miR-21, the nanomachine was quickly activated. The target miRNA (T) bound to B by a toehold-mediated strand displacement to form a B−T complex and a free W. Subsequently, W unfolded the hairpin structure of the adjacent H1 and exposed its locked toehold. Then, the H2 strand anchored on the TDN served as the fuel molecule to bind to H1 *via* a new strand-displacement reaction, resulting in the generation of a stable H1−H2 duplex and the concurrent release of the free W to initiate a new cycle along the ACSP track. As a result of the 3D walking amplification, multiple TDNs were assembled on the surface of the ACSPs to form ACSP-TDN core satellite nanostructures through repeated unfolding, binding, and release cycles. The rigid structure of duplex H1−H2 prevented the Cy5-tag on H1 from getting close to the ACSP surface during the autonomous assembly process, while the Rox-tag on H2 remained in proximity to the ACSP surface. It is worth mentioning that these effective position changes triggered a continuous Cy5 fluorescence signal recovery and Rox fluorescence quenching, while the prominent Rox and Cy5 SERS signal outputs were reduced. By virtue of this design, the amplified ratio signals of Rox to Cy5 in different modes could be cross-referenced for accurate detection of intracellular miR-21 and more comprehensive imaging monitoring in live cells. Furthermore, under 808 nm laser irradiation, ACSPs could also act as multifunctional nanoagents to generate hyperthermia and highly toxic ROS in the tumor microenvironment (TME), which could irreversibly damage biomolecules and result in cellular apoptosis or necrosis.

Construction and Characterization of nACSPs. The main synthesis procedure of nACSPs is illustrated in Figures 1A and S1. First, spherical monodisperse gold nanoparticles (AuNPs) were synthesized. Then, they were dispersed in an aqueous polyvinylpyrrolidone solution, which was employed to improve the Au-core NP stability and assist in the *in situ* self-assembly. Subsequently, cupric sulfate pentahydrate, thioacetamide, and hydroxylamine hydrochloride were sequentially added, and the Au@$Cu_{2-x}S$ core−shell nanostructures (ACSNs) were synthesized *via* a modified self-assembly protocol.[46] Polydopamine (PDA) possesses a versatile bioconjugation ability, outstanding fluorescence quenching effect, and high photothermal performance. Therefore, the ACSN surface was further coated with a PDA shell by *in situ* emulsion polymerization to construct Au@$Cu_{2-x}S$@PDA nanoparticles (ACSPs). The thiolated DNA was assembled onto the surface of the ACSPs *via* the quinone groups in the PDA shell to produce nACSPs.

Transmission electron microscopy (TEM) images revealed that the diameter of the visually red Au NPs was approximately 15 nm (Figure 1B). The ACSNs appeared as uniform and well-dispersed core−shell spheres with an average size of approximately 35 nm (Figure 1C). As revealed by the high-resolution TEM (HRTEM) images, the $Cu_{2-x}S$ shell featured distinct lattice fringes, indicating high crystallinity (the inset in Figure 1C). Figure 1E shows its energy dispersive spectrometer (EDS)-elemental mappings. The Au, Cu, and S element distributions further confirmed the dual plasmonic core@shell

https://doi.org/10.1021/acsnano.0c10844
ACS Nano 2021, 15, 6961−6976

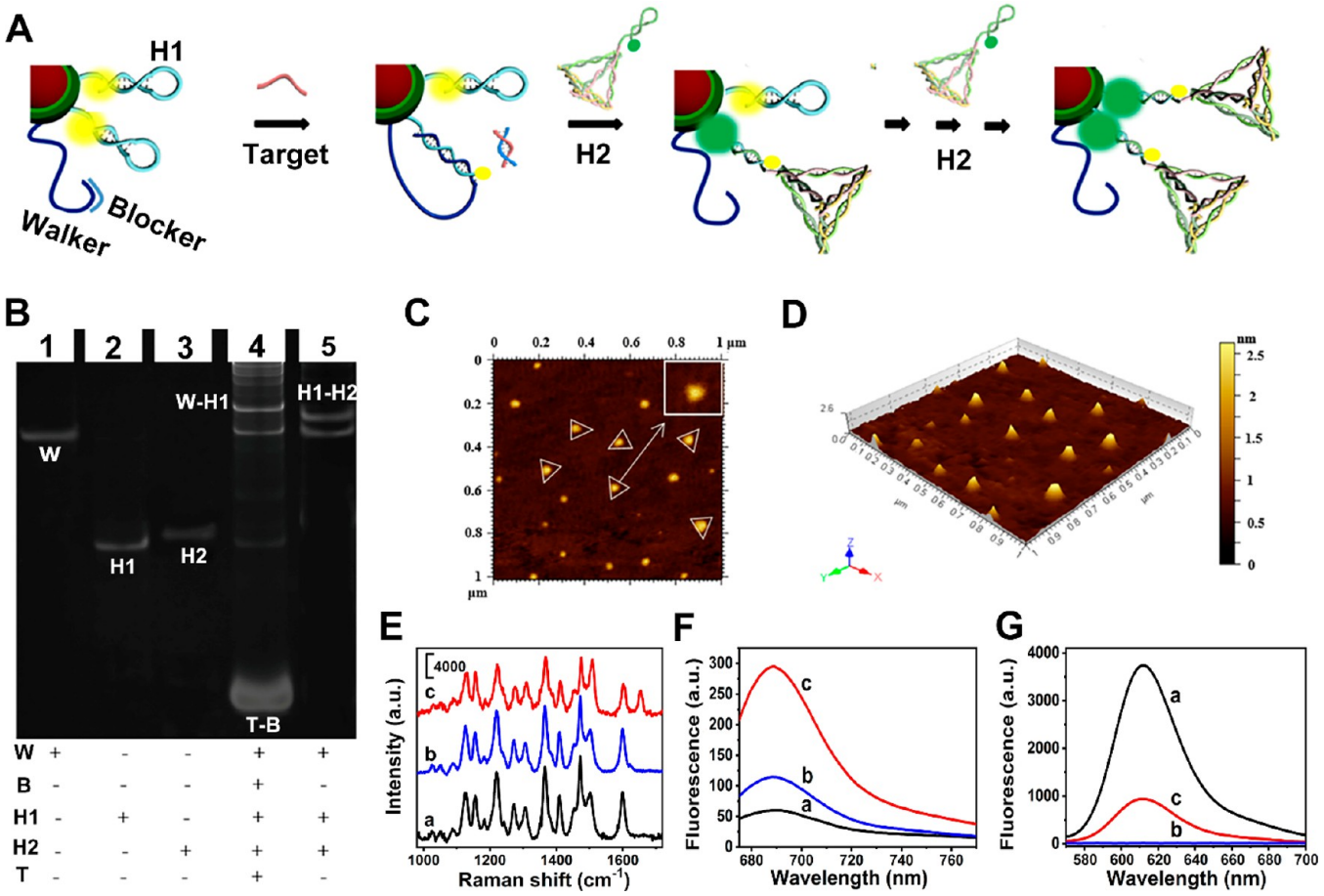

Figure 2. Feasibility of the ratiometric SERS-FL dual-spectrum nanosystem. (A) Schematic illustration of the motion of the 3D DNA walking nanosystem in response to specific target. (B) Polyacrylamide gel electrophoresis image of the DNA walking reaction. (C, D) AFM imaging of TDN. (E) SERS spectra in the absence of miR-21 (a) and in the presence of 1 pM miR-21 without (b) and with (c) fTDN. (F, G) Fluorescence spectra of Cy5 (F) and Rox (G) in the absence of miR-21 (a) and in the presence of 10 nM miR-21 without (b) and with (c) fTDN.

nanostructure. With the self-polymerization of dopamine, the solution color changed from green to black, and the resulting ACSPs had a mean diameter of 45 nm and a thin PDA shell of approximately 5 nm (Figure 1D). The EDS spectrum indicated the elemental composition of the ACSPs (Figure S2), in which the N and O elements originated from the PDA shell. The characteristic peaks of PDA (3410, 1605, 1510, and 1295 cm^{-1}) in the Fourier transform infrared (FT-IR) spectrum provided additional evidence of the successful coating with the PDA shell (Figure S3A). X-ray diffraction (XRD) and X-ray photoelectron spectroscopy (XPS) were performed to assess the components and chemical status of the ACSPs. The XRD pattern contained the characteristic peaks of Au and $Cu_{2-x}S$ (Figure 1F). The typical Au, Cu, S, N, and O signals could be observed in the XPS spectrum (Figure S3B–H), further indicating the element composition in the ACSPs, which was consistent with the EDS results (Figure S3). In addition, the XPS spectrum of Cu 2p showed two main peaks at 952.5 and 932.6 eV (Figure S3C), corresponding to Cu $2p_{1/2}$ and Cu $2p_{3/2}$, respectively, which confirmed the coexistence of Cu^{+} and Cu^{2+}.[47,48] Both the ζ potential value change and hydrodynamic size increase indicated the successful assembly during each step (Figure 1G). The final ζ potential value and hydrodynamic particle diameter of the ACSPs were −39.7 mV and 58 nm, respectively. Regarding their chemical stability, in contrast to the ACSNs, the ACSPs showed good colloidal stability in neutral and acidic buffers (Figure S4), which could be attributed to the PDA surface coating. The optical properties of ACSN and ACSP aqueous dispersions were studied by UV−vis-NIR absorption spectra. As shown in Figure 1H, the ACSN spectrum contained two distinct SPR peaks in the visible and NIR regions (curve c). The plasmon absorption of the Au core was red-shifted by 30 nm compared to that of bare Au NPs, which was attributed to the high refractive index of the $Cu_{2-x}S$ shell. Compared with pure $Cu_{2-x}S$ NPs, there was a significant blueshift of the NIR absorption from 950 to 880 nm, which was attributed to plasmonic resonance coupling between the Au core and the $Cu_{2-x}S$ shell. The ACSPs (curve d) had a similar plasma resonance curve to the ACSNs, with a slight blueshift in the NIR absorption band, suggesting that the PDA coating may have promoted the coupling between the Au core and $Cu_{2-x}S$ shell. The SERS activity of the aforementioned NPs assembled with 5′-thiolated and 3′-Cy5 tagged hairpin DNA (H1) was evaluated next. As shown in Figure 1I, the strong SERS response was observed on ACSPs (curve d). The Raman peak at 1602 cm^{-1} originated from the C═N stretching vibrations of the Cy5 molecule on DNA H1. The SERS enhanced factor (EF) values for Cy5 on AuNPs, ACSNs, and ACSPs were estimated to be 3.69×10^6, 7.01×10^6, and 1.06×10^7,

https://doi.org/10.1021/acsnano.0c10844
ACS Nano 2021, 15, 6961−6976

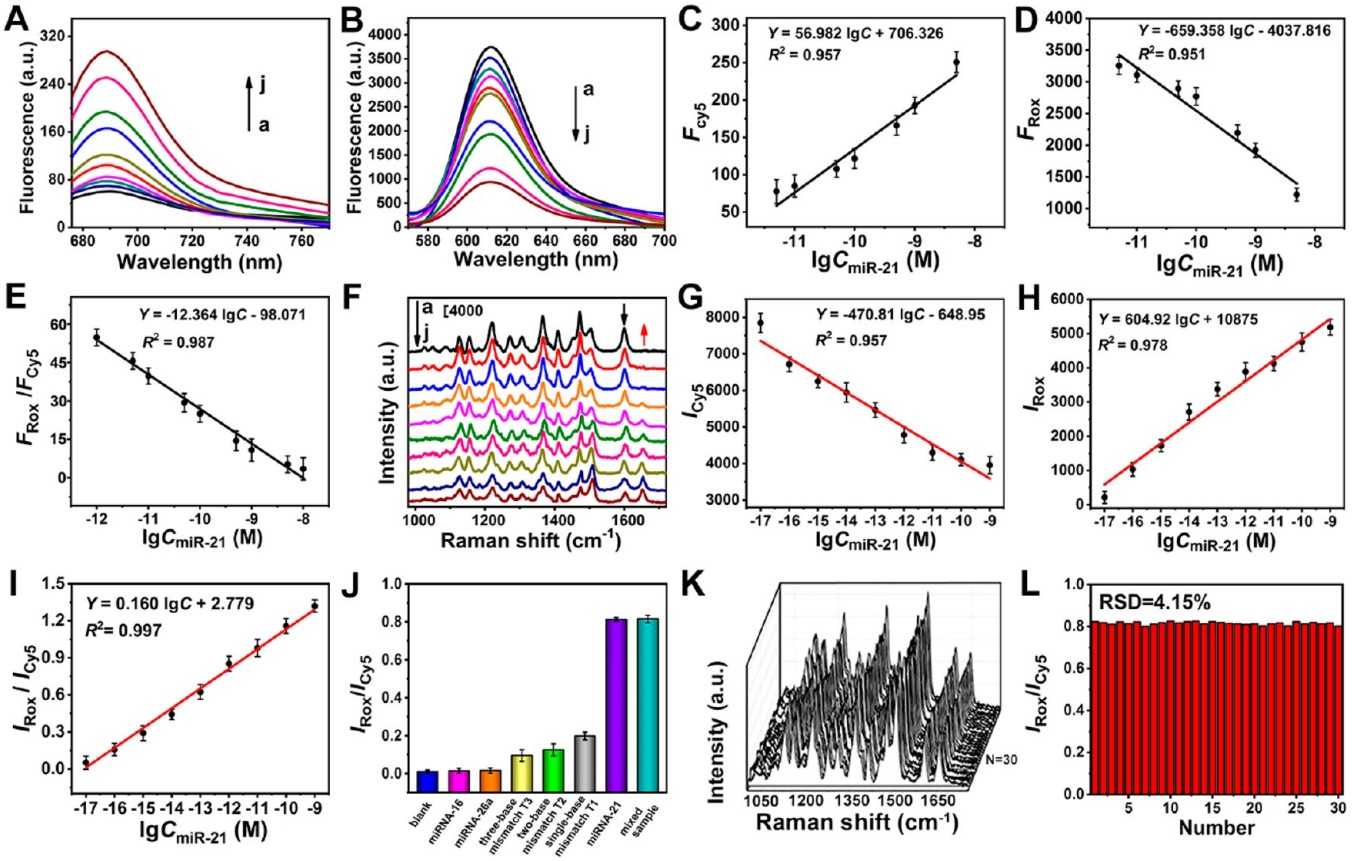

Figure 3. Ratiometric SERS-FL dual-spectrum nanomachine for miR-21 detection *in vitro*. (A–E) Fluorescence spectra of Cy5 (A), Rox (B) in response to miR-21 at various concentrations and their corresponding calibration curves (C and D) and ratiometric values of fluorescence intensity (F_{Rox} /F_{Cy5}) for the analysis of different concentrations of miR-21 (E). From (a) to (j): 0 pM, 1 pM, 5 pM, 10 pM, 50 pM, 100 pM, 0.5 nM, 1 nM, 5 nM, and 10 nM miR-21. (F–I) SERS spectra in response to miR-21 at various concentrations (F) and their corresponding calibration curves (G and H) and ratiometric values of SERS intensity (I_{Rox}/I_{Cy5}) for the analysis of different concentrations of miR-21(I). From (a) to (j): 0 aM, 10 aM, 100 aM, 1 fM, 10 fM, 100 fM, 1 pM, 10 pM, 100 pM, and 1 nM miR-21. (J) Specificity of the ratiometric SERS sensing system for miR-21. The concentrations of miR-21 and other different microRNAs were 1 pM and 5 pM, respectively. (K, L) SERS mapping spectra of the ratiometric SERS sensing system for 1 pM miR-21 collected from 30 random spots on the detection chip (K) and corresponding ratiometric SERS values (L).

respectively, confirming that the ACSPs had the strong Raman enhancement ability among them. The LSPR-induced electromagnetic field enhancement is a key factor for SERS signal enhancement. Finite difference time domain (FDTD) calculations were performed to investigate this property (Figures 1J and S5). The results showed that compared to the pure AuNPs and the ACSNs, the ACSP nanoprobe produced a higher electric field intensity and larger area of electric field enhancement due to stronger LSPR coupling, which was consistent with the UV–vis-NIR spectroscopy experiment results (Figure 1H). On the other hand, the abundant quinone groups in the PDA nanoshell are highly reactive toward thiol groups, and the functionalized biomolecules can be covalently immobilized on the surface through Schiff base or Michael addition reactions.[49−51] The PDA surface coating resulted not only in a stronger binding capacity of the ACSPs but also a larger surface area for anchoring of the signal probe, leading to a significantly increased probe molecule loading efficiency and further enhancement of the Raman signal. Furthermore, the SERS signal of Cy5 on the nACSP nanoprobe showed a negligible decline even after 7 days of storage (Figure 1I, curve e), indicating that the chemical stability of the PDA nanoshell could contribute to maintaining the spectral activity. The ACSPs were also used as nanoquenchers because of the robust fluorescence quenching ability of PDA.[52,53] As shown in Figure S6, free Cy5-labeled H1 had a strong fluorescence emission at 688 nm, while the fluorescence signals of the Cy5-H1 functionalized ACSPs were negligible, demonstrating the high fluorescence quenching efficiency of the ACSPs. The above results revealed the excellent optical properties of the ACSP nanoprobe.

Feasibility of the Ratiometric Dual-Spectrum Nanosystem. Several experiments were performed to investigate the feasibility of the proposed nanosystem. The operation process of the target-triggered 3D DNA walker nanodevice is indicated in Figures 2A and S7. A DNA analog of the miRNA target based on the same base-pairing recognition and signal response was used in the following *in vitro* experiments. First, the catalytic feasibility of the walking amplifier was verified by polyacrylamide gel electrophoresis (PAGE). As shown in Figure 2B, there was only one band in lanes 1–3, indicating that H1, H2, and W were pure, and no catalytic assembly occurred. Two new bands, T–B and W–H1, were observed in lane 4 (W–B+T+H1), suggesting that the walking ability of W could be activated by targeted binding. In the walking system, W could be recycled with the formation of the H1–H2 complex. The appearance of the H1–H2 band in lane 5

https://doi.org/10.1021/acsnano.0c10844
ACS Nano 2021, 15, 6961–6976

indicated the catalytic performance of the walker. Next, successful formation of TDN and fTDN was characterized by a gradual decrease in the gel mobility with sequential addition of oligonucleotides from TDNa to H2 (Figure S8). The vertebral shape of TDN with a size of 2 nm was further visualized by atomic force microscopy (AFM, Figures 2C,D and S9). The TDN performed three important functions in this system. One function was loading the H2 fuel probes to distance the Rox tag from the ACSPs, effectively preventing background interference. A second function was to improve the cell internalization efficiency of the hairpin probe. Last, TDN protected the hairpin probe against enzymatic degradation, enhancing the biological stability of the probe.[11,54] Then, dual SERS and fluorescence measurements were performed to test the amplification operation of the nanodevice during the activating, unfolding, and releasing processes. As shown in Figure 2E, the proposed nanoprobe (nACSP) worked well in the presence of the target and fTDN, with a strong Rox/Cy5 SERS output (curve c). However, only a slight signal change was obtained in the absence of the fTDN, even if H1 was unfolded by the activated W, because the walking amplifier could not operate without H2 as fuel (curve b). The ratio fluorescence detection further confirmed the amplification feasibility of the nanodevice (Figure 3F,G). As anticipated, the nanodevice produced a high-fluorescence ratio signal only when the walking probe was effectively operated with the fuel probe. With the addition of the target, the fluorescence intensity of Cy5 at 688 nm increased and that of Rox at 612 nm decreased. The above results were consistent with our postulated mechanism of the nanomachine, demonstrating the feasibility of the dual-ratiometric dual-spectrum nanosystem for the detection of miRNAs.

Performance Evaluation of miRNA Detection *In Vitro*. To achieve the best analytical performance, a series of experimental conditions, such as the length of walker DNA and blocker DNA, the concentration ratio of W to H1, and the walking time of W, were optimized (Figure S10). Under the optimum conditions, the sensitivity of the ratiometric dual-spectrum nanosystem was investigated. As shown in Figure 3A,B, with increasing target concentration, the fluorescence intensity of Cy5 (F_{Cy5}) at 688 nm increased gradually, while the fluorescence intensity of Rox (F_{Rox}) at 612 nm decreased correspondingly. Figure 3C,D shows the linear relationship between the fluorescence intensities and the logarithm of the target concentration ranging from 5 pM to 5 nM. The limit of detection (LOD) was 4.78 pM with an R^2 of 0.957 (for the Cy5 signal) and 1.12 pM with an R^2 of 0.951 (for the Rox signal; 3σ). To achieve a higher accuracy and sensitivity, ratiometric measurements were utilized to detect miR-21 by calculating the ratio of F_{Rox}/F_{Cy5}. Excellent linearity between the ratiometric signals and the logarithmic concentration of miR-21 in the range from 1 pM to 10 nM was achieved (Figure 3E). The corresponding regression equation was $Y = -12.364 \log C - 98.071$, with a good correlation coefficient R^2 of 0.987, where Y and C represent the fluorescence ratiometric signals and the correlation concentration of miR-21, respectively. Significantly, the LOD of the fluorescence ratio detection was calculated to be 0.11 pM based on 3σ, which was approximately 43.5-fold lower than that achieved by F_{Cy5} and 10.2-fold lower than that achieved by F_{Rox} alone. Figure 3F shows the response of the SERS mode to the variation of the target concentration. The typical peaks of Cy5 at 1602 cm^{-1} and of Rox at 1644 cm^{-1} were used to quantitatively evaluate the SERS response of miR-21. Increasing the miR-21 concentration caused the Raman intensity to decrease for Cy5 (I_{Cy5}) and increase for Rox (I_{Rox}). I_{Cy5}, I_{Rox}, and I_{Rox}/I_{Cy5} all varied linearly with the logarithmic concentration of miR-21 in the 10 aM to 1 nM range (Figure 3G–I). The LODs of the I_{Rox}/I_{Cy5} ratio mode and individual I_{Cy5} and I_{Rox} mode were estimated to be 4.95 aM, 5.82 aM and 6.47 aM, respectively. These results indicated that the sensitivity of the SERS platform for target miRNA was much higher than that of fluorescence analysis. More significantly, the dual SERS and FL ratiometric strategies both exhibited better linear relationships with the miR-21 concentration and lower LOD than those achieved by using either the corresponding Cy5 signal or Rox signal alone. Furthermore, to the best of our knowledge, the LOD obtained in our SERS ratiometric strategy is much lower than that of other methods used for miRNA detection.[11,16,55−57] The excellent sensitivity could be attributed to the following factors. First, in the target-triggered 3D DNA walker cascade amplification system, each target miRNA could activate the autonomous assembly on the nanomachine and generate large amounts of signal output, effectively improving the detection performance. Second, the robust SERS enhancement and fluorescence quenching ability of the ACSPs may provide a high signal-to-noise ratio. Third, adopting TDN to load fuel probes can reduce nonspecific adsorption and background signals.

The selectivity of the nanodevice was also investigated. As shown in Figure 3J, compared with the blank control, only the mixed samples and target miRNA could induce high-intensity Raman responses. In contrast, the I_{Rox}/I_{Cy5} signals for two-base mismatched T2 and single-base mismatched T1 were only about 15.2% and 24.3% of target responses, respectively. Similar trends were observed in the ratio fluorescence analysis (Figure S11), highlighting the excellent selectivity of the nanodevice. The SERS response was recorded for 30 random spots (Figure 3K), and the relative standard deviation (RSD) of the ratiometric Raman signals was 4.15% (Figure 3L), demonstrating the good reproducibility of the proposed nanosystem. Anti-interference ability and signal stability are important parameters in the performance evaluation of any analysis platform. To test this hypothesis, our nanodevice was incubated with buffer, 10% fetal bovine serum (FBS), bovine serum albumin (BSA), glutathione (GSH), and 0.5 U mL^{-1} DNase I for 6 h. As shown in Figure S12, few changes in the SERS or fluorescence ratio signals were observed compared to the background, which was consistent with previous reports,[11,53] indicating that the developed nanomachine could effectively avoid false positive signals caused by enzymatic degradation and other biomolecular interference due to the protection provided by the PDA shell and the tetrahedral backbone. Next, the influence of temperature and pH fluctuations on the proposed sensor performance was evaluated. Employing the ratiometric signal readout mode, no significant Rox/Cy5 value changes were observed either in SERS or in fluorescence detection (Figure S13), suggesting the high signal stability of the nanomachine. More compelling, when the walking amplification products were treated with HeLa cell lysates, the SERS signal ratio remained stable for 8 h with little change (Figure S14A), which may be attributed to the dual protective effects of ACSPs and TDN. Similar results were also obtained in the ratio fluorescence analysis (Figure S14B). The excellent stability, as well as a ratio-based signal output strategy, efficiently improved the analysis accuracy,

https://doi.org/10.1021/acsnano.0c10844
ACS Nano 2021, 15, 6961−6976

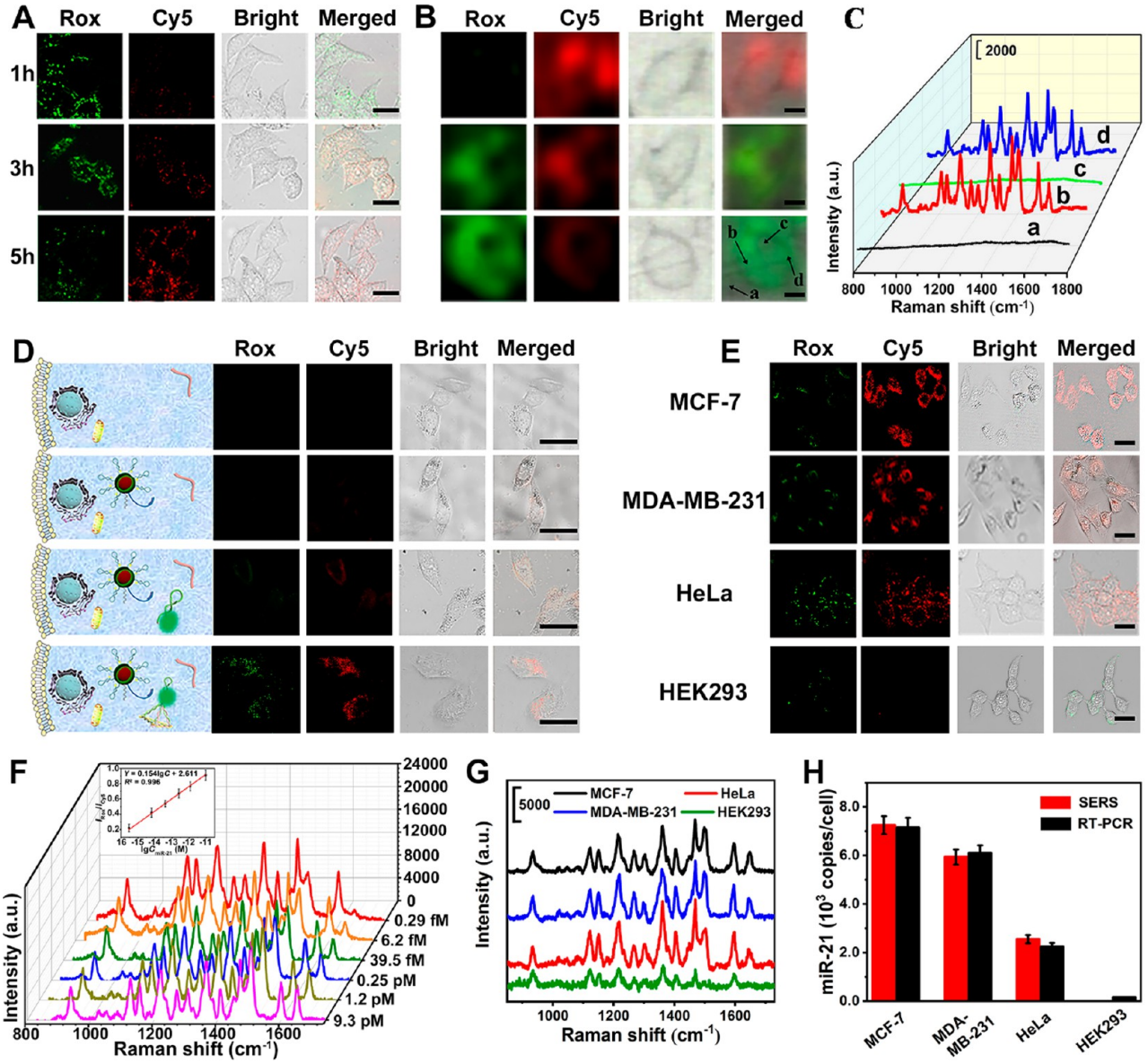

Figure 4. (A) Confocal fluorescence images of nanomachine incubated with HeLa cells. Scale bar: 20 μm. (B) SERS images of nanomachine incubated with HeLa cells. Scale bar: 10 μm. (C) Representative Raman spectra at different locations indicated in (B), including the surrounding environment (a), cytoplasm (b, d), and cell nucleus (c). (D) Fluorescence images of miR-21 in living HeLa cells without treatment and incubated with nACSPs, nACSPs/H2, and nACSPs/fTDN for 5 h. Scale bar: 40 μm. (E) Confocal fluorescence images of miR-21 in MCF-7, MDA-MB-231, HeLa, and HEK293 cells. Scale bar: 40 μm. (F) SERS spectra of miR-21 in HeLa cells with the nACSP-fTDN nanodevice. Inset: SERS ratiometric intensity (I_{Rox}/I_{Cy5}) *versus* intracellular contents of miR-21. (G) SERS spectra of MCF-7, MDA-MB-231, and HeLa cells with nACSP-fTDN nanodevice. (H) Quantification of miR-21 in different tumor cell lines through SERS spectra and qRT-PCR.

indicating the great potential of the walking nanodevice for its application in the detection of target miRNA in living cells.

Imaging and Quantitative Analysis of miR-21 in Living Cells. Intracellular miRNA imaging was performed using a human cervical cancer cell line (HeLa) overexpressing miR-21.[24,58,59] Prior to application of the 3D walking nanosystem to living cells, the cytotoxicity of the nACSPs and fTDN was tested by a standard 3-(4,5-dimethylthiazol-2-yl)-2,5-diphenyl-tetrazolium bromide (MTT) assay. The culture solution group was used as the control. As shown in Figure S15, after incubation with the nACSP/fTDN mixture for 36 h, three cancer cells (MCF-7, MDA-MB-231, and HeLa) and three normal cells lines (HEK293, L02, and L929) all presented relatively high viability, confirming the excellent biocompatibility of the proposed nanosystem. Then, the feasibility of the nanosystem operation in HeLa cells was assessed by monitoring the SERS mapping and fluorescence imaging signals at different incubation times in living cells. In the confocal fluorescence image, green fluorescence originated from Rox, indicating that the fTDN probe was internalized into the HeLa cells. The red fluorescence was derived from Cy5 fluorescence recovery, suggesting that hairpin H1 was unfolded and that the walking amplifier was activated through targeted recognition. Subsequently, red fluorescence signals in HeLa cells were observed. Upon prolonging the incubation time, the red fluorescence gradually increased, and an intense fluorescence signal was observed at 5 h (Figure 4A). The SERS mapping results were consistent with the fluorescence studies.

https://doi.org/10.1021/acsnano.0c10844
ACS Nano 2021, 15, 6961−6976

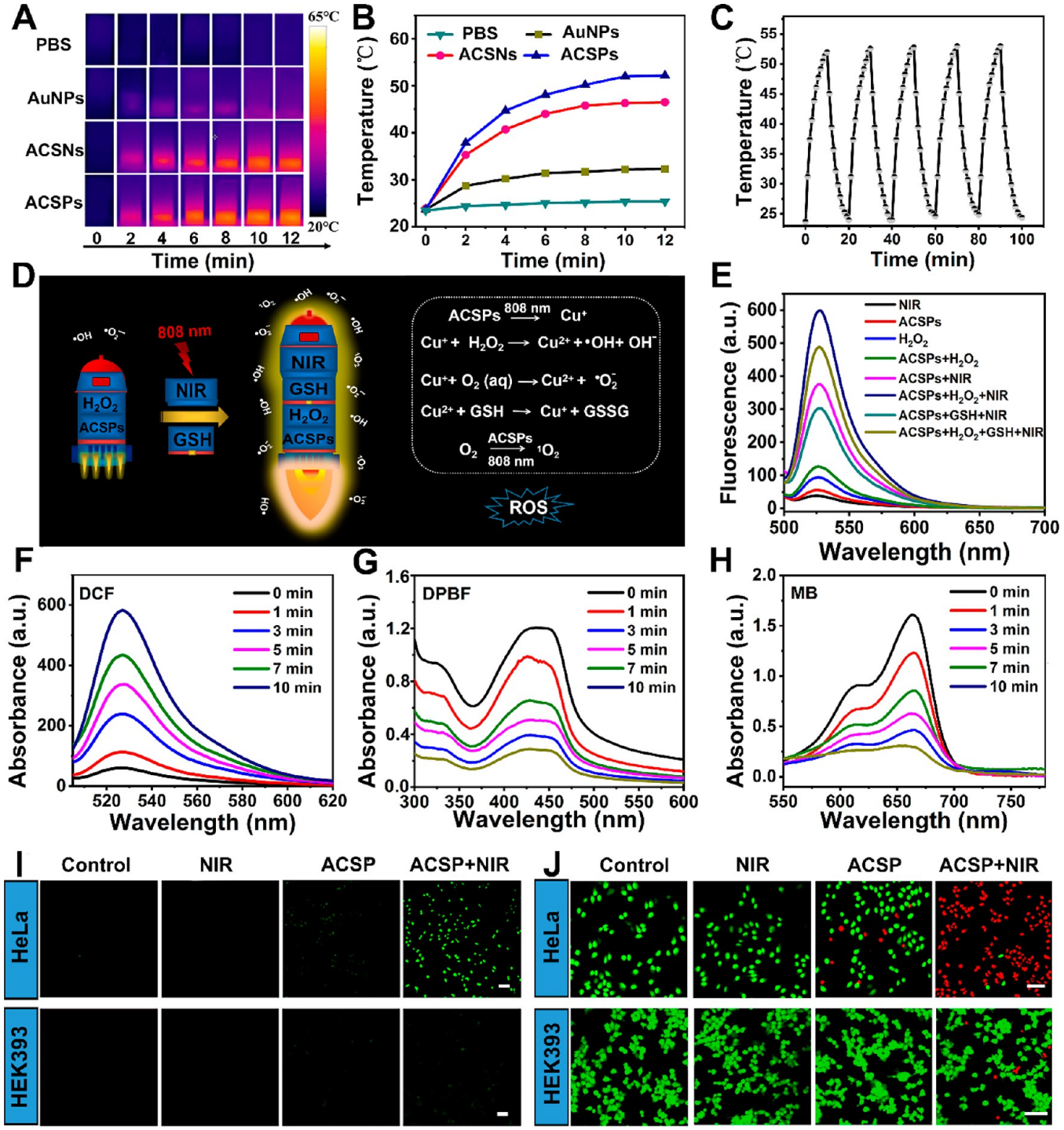

Figure 5. Photothermal performance and ROS effect of ACSPs *in vitro*. (A, B) Infrared thermal images (A) and corresponding temperature rise curves (B) of PBS, AuNPs, ACSNs, and ACSPs under 808 nm laser irradiation (1.3 W cm^{-2}). (C) Photothermal stability of ACSPs (five irradiation on/off cycles) under 808 nm laser (1.3 W cm^{-2}). (D) Schematic illustration of ROS generation and GSH depletion of ACSPs. (E) Fluorescence spectra of DCF caused by ROS production: (a) PBS + NIR, (b) ACSP, (c) H_2O_2, (d) ACSP + H_2O_2, (e) ACSP + NIR, (f) ACSP + H_2O_2 + NIR, (g) ACSP + GSH + NIR, and (h) ACSP + H_2O_2 + GSH + NIR. (F) Fluorescence spectra of DCF incubated with ACSPs (200 μg mL^{-1}) and H_2O_2 (1 mM) upon different irradiation time (t = 0−10 min) of 808 nm laser. (G) Degradation of DPBF due to $\cdot O_2^-$ and $^1O_2$ generation: 200 μg mL^{-1} of ACSPs with 1 mM H_2O_2 at different irradiation times. (H) Degradation of MB caused by ·OH production: 200 μg mL^{-1} of ACSPs with 1 mM H_2O_2 at different illumination times. (I) Fluorescence images of DCFH-DA-stained HeLa and HEK293 cells with different treatments. (J) Fluorescence images of AO/EB costained HeLa and HEK293 cells. Scale bar: 100 μm.

With the activation of the amplification reaction, the green field of Rox was continuously enhanced and was the brightest at 5 h (Figure 4B). Furthermore, the SERS spectra obtained from different sites in single HeLa cells showed that the target miRNA-triggered amplification reaction mainly occurred in the cytoplasm, which was consistent with colocalization fluorescence imaging analysis of nuclear staining with DAPI (Figures 4 C and S16). Both SERS mapping and fluorescence imaging

https://doi.org/10.1021/acsnano.0c10844
ACS Nano 2021, 15, 6961−6976

were in perfect agreement with the proposed working mechanism. However, SERS imaging required at least 10 min. In contrast, fluorescence imaging was much faster and required only a few seconds. Thus, the cell penetrability and amplification efficiency of the proposed walking nanodevice were visualized by fluorescence imaging. The HeLa cells were incubated with nACSPs, nACSPs/H2, and nACSPs/fTDN for 5 h. As shown in Figure 4D, with the addition of nACSPs only, a weak Cy5 fluorescence signal was observed because H1 was unfolded by the miR-21-triggered strand displacement reactions at a ratio of 1:1 without signal amplification. Subsequently, even when the free fuel molecule H2 was added, very weak Rox fluorescence was observed, but the Cy5 signal was not significantly enhanced. This result suggested poor penetrability and low biostability of the free hairpin DNA. Notably, after incubation with the nACSP/fTDN mixture, Rox and Cy5 fluorescence could be observed in the HeLa cells. These results indicated that the excellent self-delivery efficiency of the proposed nanodevice without the help of transfection agents and demonstrated the high amplification ability for *in situ* imaging of microRNA in living cells.

Dynamic identification of miRNA expression levels is of great significance for clinical diagnosis, targeted therapy, and prognosis monitoring. Treatment of HeLa cells with miRNA21 mimics or inhibitors could upregulate or downregulate intracellular miRNA expression. As shown in Figure S17, with untreated HeLa cells as the control group, the Rox signal was weaker, and the Cy5 fluorescence signal was stronger in the mimic treatment group, while a brighter Rox fluorescence signal and less intense Cy5 fluorescence were observed in the inhibitor treatment group. The results indicated that the proposed nanodevice could accurately monitor changes in the miRNA expression levels in living cells. Then, three cancer cells (MCF-7, MDA-MB-231, and HeLa) and a normal cell (HEK293) were selected to evaluate the practical applicability of the presented approach. Confocal imaging results (Figure 4E) revealed higher miR-21 expression levels in MCF-7 cells and MDA-MB-231 cells than in HeLa cells, which was consistent with previous reports.[9,11,60] However, in HEK293 cells, the Rox fluorescence signal was extremely weak, while Cy5 fluorescence was almost unobservable, which may be due to the lower expression of miR-21 and nucleolin negative expression in normal cells compared with tumor cells.[59,61] Moreover, based on the higher sensitivity of SERS signal, the designed nanodevice was further used for the quantitative analysis of intracellular miR-21 with SERS spectra, and the dual-signal ratio strategy provided high accuracy in the biological matrix. As shown in Figure 4F, the ratio SERS intensity of I_{Rox}/I_{Cy5} showed a good linear relationship with the logarithmic concentration of miR-21 in the cells from 0.29 fM to 9.30 pM with LOD of 0.11 fM (3σ). The LOD was approximately 7-fold lower than that of the previous reports for intracellular miR-21 analysis so far (Table S2). According to the corresponding standard curve, the accurate quantification of miR-21 in the three cancer cell lines was obtained with the SERS spectra (Figures 4G and S18 and Table S3). The contents of miR-21 in HeLa, MDA-MB-231, and MCF-7 cells were calculated to be 42.0 ± 2.6 fM, 98.5 ± 4.1 fM, and 120.3 ± 5.8 fM ($(2.5 \pm 0.15) \times 10^3$, $(5.9 \pm 0.24) \times 10^3$, and $(7.2 \pm 0.37) \times 10^3$ copies/cell), respectively. For HEK293 cells, the extremely low probe signal was caused by lack of nucleolin on the cell membrane, which might block the delivery of nanomachine. These results agreed well with the fluorescence imaging results and reported data.[16,60] The above results were further confirmed by quantitative reverse transcription PCR (qRT-PCR), a conventional method (Figure 4H and Table S3). These findings demonstrated that our nanodevice could not only identify cancer cells from normal cells based on probe specificity but also distinguish different cancer cells according to different miRNA expression and realize accurate quantification of target miRNA in living tumor cells. To further confirm the feasibility of clinical application of the proposed nanodevice, the analysis of miR-21 from serum samples of three newly diagnosed cervical cancer patients was performed using standard addition method. As shown in Table S4, miR-21 at levels of 104.3 ± 4.8 fM, 132.5 ± 7.6 fM, and 113.7 ± 4.3 fM were detected in serum samples from patients, respectively. These results agreed well with those of qRT-PCR analysis, suggesting the excellent clinical application potential.

Evaluation of Photothermal Performance and ROS Effect of ACSPs *In Vitro*. The above results indicated the great potential of our proposed nanomachine in accurate diagnosis. In addition, the ACSP nanoprobes in the nanosystem could also be used as excellent nanoagents for PTT- and ROS-mediated multimodal synergistic therapy. The dual-plasmon coupling of the Au core and the $Cu_{2-x}S$ shell can not only improve the SERS effect but also enhance the photothermal performance. Coupled with the inherent photothermal properties of the PDA shell, the three photothermal agent entities (*i.e.*, AuNP, $Cu_{2-x}S$, and PDA shell) result in strong NIR absorption and a satisfying photothermal conversion efficiency of our nanoprobes. As depicted in Figure 5A,B, under 808 nm laser irradiation, the temperature of the ACSP aqueous solution could reach approximately 52.2 °C within 10 min. In contrast, under the same conditions, the temperatures of PBS, Au NPs, and ACSNs only reached 25.4, 31.6, and 46.3 °C, respectively, indicating the enhanced photothermal effect of the ACSPs. Moreover, the photothermal behavior of the ACSPs showed an irradiation power- and concentration-dependent pattern (Figure S19). Based on the heating and cooling curve and time constant (τ_s) (Figure S19), the photothermal conversion efficiency (η) of the ACSPs was determined to be 55.7%, which was superior to the ACSNs (46.8%) and many previously reported photothermal agents (Figure S20 and Table S5). Successive heating/cooling cycle tests were used to evaluate the stability of the ACSPs. As shown in Figure 5C, there was no significant deterioration in the photothermal properties after five NIR irradiation on/off cycles, indicating its stable photothermal performance. The excellent photothermal stability of the ACSPs could be attributed to the well-defined core−shell nanostructure and the uniform PDA shell coating.

A more significant property is that $Cu_{2-x}S$ in the ACSPs can act as a powerful photosensitizer and Fenton-like agent, leading to the generation of ROS.[38,39] A PDA shell and an AS1411 aptamer DNA were successively coated on the $Cu_{2-x}S$ shell to enhance the biocompatibility and target recognition ability of the ACSPs. After the ACSPs specifically accumulated on the surface of the tumor cells and were internalized by endocytosis, Cu^+ ions could be released from the ACSPs under 808 nm laser irradiation, which was attributed to the promoted degradation process at high temperature.[38,39,43] Then, Cu^+ could react with endogenous H_2O_2 to produce OH through a Fenton-like reaction and could also be oxidized by molecular oxygen (O_2) to form toxic O_2^-.[37,43,62] Both reaction processes could promote the generation of ROS and produce Cu^{2+}.

https://doi.org/10.1021/acsnano.0c10844
ACS Nano 2021, 15, 6961−6976

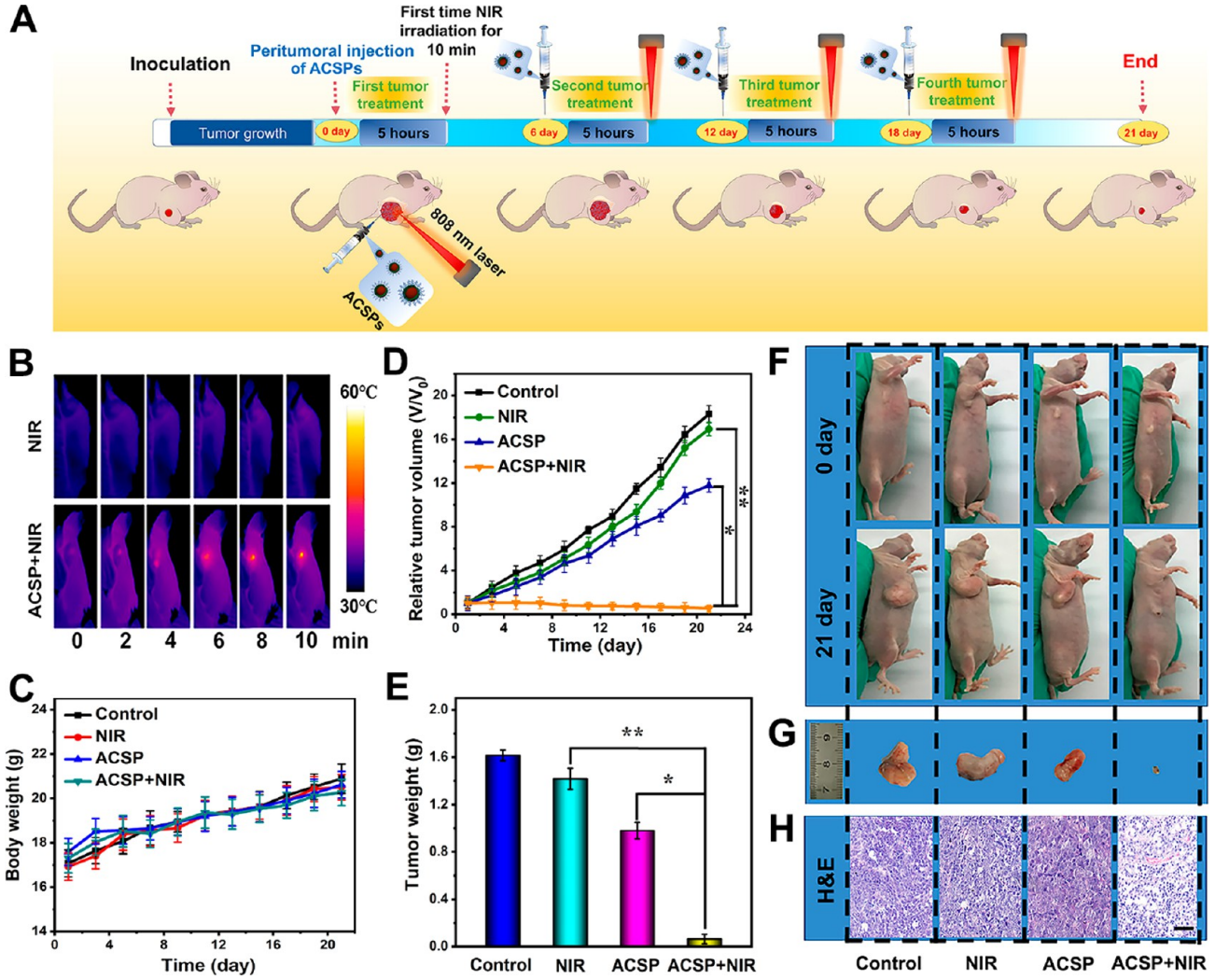

Figure 6. ***In vivo*** **antitumor efficacy of the ACSPs. (A) Schematic illustration of the tumor treatment process. (B) Photothermal images of mice bearing HeLa tumors under 808 nm irradiation (0.8 W cm^{-2}) with or without ACSPs. (C) Body weight changes of the mice in different treatment groups. (D) Relative tumor volume changes during therapy. (E) Average tumor weight with different treatments. Error bars are based on the standard deviation (SD) among five mice. Photographs of representative mice (F) and tumors (G) from different groups. (H) H&E stain assay of tumor slides from HeLa tumor-bearing mice with different treatments. *P < 0.05, **P < 0.01. Scale bar: 100 μm.**

Subsequently, the generated Cu^{2+} would be reduced to Cu^{+} by consuming excess GSH in the TME,[34,44] leading to a cyclic conversion of the two redox states (Cu^{+} and the Cu^{2+}). Moreover, the ACSPs can convert oxygen into highly toxic $^1O_2$ upon NIR irradiation.[40,63,64] The smart circulation system ensured the generation of a considerable quantity of ROS and weakened the antioxidant defenses of the tumor cells. Furthermore, the high PT conversion performance of the ACSPs could further improve the ROS generation efficiency, thereby realizing single nanoagent-mediated PTT/PDT/CDT trimodal synergistic therapy (Scheme 1B and Figure 5D). As the production of highly toxic ROS is an important factor in tumor therapy, 2,7-dichlorofluorescein (DCF) was used as a probe to investigate the ROS production capacity of the ACSPs.

As displayed in Figure 5E, no obvious DCF fluorescence signal was detected upon NIR irradiation, H_2O_2 treatment or from ACSPs alone. The fluorescence in the ACSP plus H_2O_2 group was relatively low. However, a high signal was observed in the group of ACSP with 808 nm light irradiation, and the fluorescence intensity increased gradually with increasing irradiation time (Figure 5F) and ACSP concentration (Figure S21), indicating the efficient production of NIR-activated ACSP-mediated ROS. Notably, a much higher fluorescence signal was obtained when ACSP reacted with H_2O_2 under 808 nm laser irradiation, which demonstrated that the ROS generation efficiency of the ACSPs was significantly enhanced by combining PDT with photodriven CDT (Figure 5E, curve f). GSH has a powerful scavenging effect on generated ROS.[65] Surprisingly, after the addition of GSH, the fluorescence signal of DCF with or without H_2O_2 was only slightly reduced by approximately 18.3% and 40.5%, respectively (Figure 5E, curves h and g). The high ROS retention efficiency could be attributed to Cu^{2+}-induced GSH consumption. Moreover, the Ellman assay was applied to further evaluate the GSH depletion by the ACSPs. As shown in Figure S22, under 808 nm laser irradiation, the GSH level progressively decreased upon increasing the concentration of the ACSPs. Efficient GSH consumption both deteriorates the antioxidant capability and promotes Cu^{+}/Cu^{2+} cyclic conversion, thereby improving the treatment effect. DCF fluorescence in combination with NIR irradiation was used to study the ROS-generating activity

https://doi.org/10.1021/acsnano.0c10844
ACS Nano 2021, 15, 6961−6976

of the ACSPs at different pHs (7.4, 6.0, and 5.0). Interestingly, varying the pH only changed the reaction efficiency by approximately 20% (Figure S23), indicating good reaction activity for the ACSPs over a wide pH range, unlike highly pH-dependent ferrous-based nanoagents, thereby ensuring a high efficiency of the ACSP-mediated tumor therapy.

To further understand the catalytic mechanism of the ACSPs, the type of ROS products was determined by electron spin resonance (ESR) using 5,5-dimethylpyrroline-1-oxide (DMPO) and 2,2,6,6-tetramethylpiperide (TEMP) as the spin trap agent (Figure S24), and the results indicated that the products included $\cdot O_2^-$, ·OH, and $^1O_2$. Moreover, degradation experiments of 1,3-diphenylisobenzofuran (DPBF) and methylene blue (MB) were performed to further determine the free radical products. The radical products $\cdot O_2^-$ and $^1O_2$ can degrade DPBF, whereas ·OH can degrade MB.[35,66] As shown in Figures 5G,H and S25, the absorption of DPBF and MB decreased with increasing NIR irradiation time and ACSP concentration. However, when N_2, ethanediamine (chelating agent of Cu ion), isopropanol (·OH scavenger), superoxide dismutase ($\cdot O_2^-$ scavenger), and carotene ($^1O_2$ scavenger) were added to the system, respectively, the DCF fluorescence and degradation reactions of DPBF and MB were inhibited accordingly, further confirming the efficient generation of $\cdot O_2^-$, ·OH, and $^1O_2$ (Figure S26).

Encouraged by the above results, the intracellular ROS production ability of the ACSPs was further evaluated by 2,7-dichlorofluorescein-diacetate (DCFH-DA), which produces green fluorescence after reacting with ROS. As shown in Figures 5I and S27, the green fluorescence in the HeLa cells treated with ACSP + NIR was significantly more intense than that in untreated cells or NIR- or ACSP-treated cells, whereas almost no fluorescence was observed in normal HEK293 cells with the different treatment conditions. This result indicated that the ACSPs could specifically generate a large amount of ROS in thetumor cells based on the synergistic effect of NIR-induced CDT and PDT, while the effect on normal cells was negligible due to the low cell uptake efficiency of the ACSPs and the low H_2O_2 expression in normal cells. This enables the ACSPs to selectively kill tumor cells and reduce the side effects to normal cells. Furthermore, the anticancer effect of the ACSPs under different conditions was further evaluated by MTT analysis (Figure S28). As expected, the HeLa cells treated with ACSP + NIR exhibited the lowest viability at all concentrations, indicating that the ACSPs could effectively combine PTT with PDT and CDT triggered by NIR irradiation to obtain the best anticancer effect. Normal cells, however, could still maintain at least 78% viability under the same conditions, showing few side effects. In addition, an acridine orange/ethidium bromide (AO/EB) staining experiment more intuitively demonstrated the ability of the ACSPs to selectively kill tumor cells under NIR irradiation. As displayed in Figure 5J, the ACSP + NIR-treated HeLa cells showed a strong apoptotic signal, which was visually evidenced by the red staining of dead cells by EB compared with the bright green fluorescence in normal 293T cells. Flow cytometry analysis also verified the excellent therapeutic effects of the ACSPs upon NIR irradiation (Figure S29). Collectively, these results indicated that the ACSPs show great potential as all-in-one nanoagents for PTT/PDT/CDT synergistic therapy.

***In Vivo* Antitumor Efficacy of the ACSPs in Multiple Modes.** Based on the good antitumor efficacy of the ACSP nanoprobe *in vitro*, *in vivo* experiments were then carried out using HeLa tumor-bearing nude mice (Figure 6A). First, the photothermal effect of the ACSPs *in vivo* was evaluated by a thermal imager. As shown in Figures 6B and S30, under 808 nm laser irradiation, the temperature at the tumorsite with peritumoral injection of ACSPs increased to approximately 60 °C within 10 min compared to that with peritumoral injection of PBS, demonstrating the effectiveness of ACSPs for photothermal treatment and thermal imaging. Then, tumor-bearing nude mice were randomly divided into four groups: control, NIR, ACSP, and ACSP + NIR (n = 5 for each group). The tumor volumes and body weights were recorded every 2 days during treatment. As shown in Figure 6C, only small weight changes in the mice were observed in response to the different treatments, indicating the high therapeutic safety of the ACSPs. In addition, Figure 6D shows that compared with the control group and the near-infrared group, the tumor growth in the ACSP group was slightly inhibited after 21 days of treatment, perhaps due to the small CDT effect of the ACSPs in the TME. Surprisingly, the mice treated with ACSP injection and 808 nm irradiation displayed the strongest tumor-suppressing effect among all the groups, with a tumor volume reduction of 48.6%, which may be attributed to the photoinduced PTT/PDT/CDT multimodal synergistic therapy. The tumors were removed from the mice at the end of the treatment and weighed. As displayed in Figure 6E, the ACSP + NIR-treated group had the smallest tumor weight, with a tumor suppression rate of 96.1%, which further illustrated the high efficiency of synergy therapy. Moreover, photographs of representative mice and their tumors more intuitively indicated that the ACSP + NIR treatments had the strongest antitumor effect in all experimental groups (Figure 6F,G), which was consistent with the results of *in vitro* cell experiments. Hematoxylin and eosin (H&E)-stained images showed a large area of tumor cell necrosis and apoptosis that occurred in response to the light-driven collaborative treatment scheme, indicating the most substantial tumor damage among the groups (Figure 6H). In addition, H&E-stained images of the major organs (including heart, lungs, spleen, liver, and kidneys) showed similar well-defined cell morphology and no obvious pathological abnormalities compared with the control group (Figure S31). Furthermore, the *in vivo* systemic toxicity of ACSPs was further assessed by injecting the healthy mice through the tail vein. The blood biochemical tests and blood routine analysis were performed on days 1, 7, and 21, respectively (Figures S32 and S33). There was no significant variation compared to the control group with saline injection. These results demonstrated the excellent clinical application potential of ACSPs with a high anticancer effect and good biocompatibility.

CONCLUSIONS

In summary, we successfully developed an intelligent theragnostic nanosystem, in which the constructed ACSP nanoprobe plays multiple important roles in synergistic tumor therapy as well as *in situ* SERS-FL monitoring. Combining fTDN-assisted walking amplification with the significant SERS enhancement and fluorescence quenching performance of the ACSP probe resulted in the successful application of the proposed nanomachine to the *in situ* imaging of miR-21 in cancer cells with high sensitivity and selectivity. Moreover, the ratio sensing strategy improved the detection reliability, and the SERS-FL dual-spectrum analysis provided complementary and substantial information for accurate diagnosis. Upon 808

https://doi.org/10.1021/acsnano.0c10844
ACS Nano 2021, 15, 6961−6976

nm laser irradiation, the ACSPs produced both excellent photothermal effects and highly toxic ROS in the tumor microenvironment, thereby realizing single nanoagent-mediated PTT/PDT/CDT synergistic therapy. The excellent antitumor efficacy was confirmed by *in vivo* and *in vitro* experiments. Therefore, this smart nanosystem, which integrates multimodal imaging with synergistic therapeutic effects, exhibits considerable potential for clinical diagnosis and cancer treatment.

EXPERIMENTAL DETAILS AND METHODS

Preparation of the nACSPs. The nucleic acid-functionalized ACSPs were prepared as follows. First, 10 μL each of 1 μM swing arm DNA (W) and 1 μM blocker DNA (B) were added to TNaK buffer (20 mM Tris, 14 mM NaCl and 5 mM KCl, pH = 7.5) at 90 °C for 5 min to synthesize walker DNA (W−B). Hairpin DNA (H1) (10 μL, 10 μM) was heated in a 90 °C water bath for 5 min and then cooled to room temperature. W−B and H1 were treated separately with 10 mM TCEP buffer (10 mM TCEP, 10 mM Tris-HCl, 1 mM ethylenediaminetetraacetic acid, 50 mM NaCl, pH = 7.4) for 1 h at room temperature. The treated W−B and H1 were added in a 1:10 molar ratio to 1 mL of ACSP solution. The mixture was isothermally incubated at 37 °C for 12 h, washed three times using 10 mM PBS buffer (NaH_2PO_4 and Na_2HPO_4, pH = 7.4), and finally dispersed in 80 μL of PBS buffer (10 mM, pH = 7.4).

***In Vitro* FL and SERS Measurement.** Different concentrations of miRNA-21 (10 μL) were reacted with the nanodevice (1 μM) for 2 h at room temperature. The reacted complex was centrifuged at 13,000 r min^{-1} for 15 min and finally dispersed in PBS buffer for SERS detection and fluorescence detection. The fluorescence spectra were determined by setting the excitation and emission slits set to 5.0 and 10.0 nm band passes. The Rox excitation wavelength was 550 nm, and the emission spectra were recorded between 570 and 630 nm. The Cy5 excitation wavelength was 635 nm, and the emission spectra were recorded between 640 and 700 nm. A 633 nm excitation light source was used to obtain the SERS spectra (where the excitation energy was fixed at 5 mW by using a neutral density filter throughout the experiment). The detection capability of this method was evaluated by monitoring the changes in the fluorescence peaks (612 and 688 nm) and Raman peaks (1644 and 1602 cm^{-1}) of Rox and Cy5, respectively. Quantitative detection of miR-21 in cells, miR-21, and antisense sequences of miR-21 was carried out by transfecting HeLa cells for 48 h. The Hela cells were incubated with the nanodevice for an additional 5 h, after which the SERS intensity was measured.

Confocal Fluorescence Imaging. Before conducting the experiment, HeLa cells, MCF-7 cells, MDA-MB-231 cells, and HEK293 cells were cultured in 96-well glass-bottom plates for 24 h at 37 °C. Then, 20 μL of dispersed nACSPs and 40 μL of fTDN were added to the cells for 2 h. The cells were washed twice with PBS. The cells were incubated for a prescribed period of time. To detect miR-21 in cells, miR-21 and antisense sequences of miR-21 were transfected into HeLa cells for 48 h. The Hela cells were incubated with the nanodevice for an additional 5 h, and fluorescence imaging was performed using a Leica TCS SP5 inverted confocal microscope. The excitation light sources of fluorescence groups Cy5 and Rox were 633 and 514 nm, respectively, and different fluorescence signals were captured for imaging using 640−700 nm and 540−640 nm channels, respectively.

***In Vitro* ROS Detection.** We used DCFH as a ROS probe to evaluate the photodynamic properties of the nACSPs. Briefly, a suspension of 1 mL of nACSPs at different concentrations (0, 50, 100, 200, and 400 μg mL^{-1}) and 100 μL of DCFH were dissolved in ethanol and H_2O_2. The suspensions were exposed to 808 nm irradiation for different periods of time (0, 1, 3, 5, 7, and 10 min) and centrifuged to remove the nACSPs. A fluorescence analyzer was then used to measure the fluorescence intensity of DCF at 520 nm.

Animal and Tumor Model. All animal studies were conducted in accordance with the Guide for the Care and Use of Laboratory Animals (Ministry of Science and Technology of China, 2006) and the Guide for the Care and Use Committee of the Animal Experiment Center of Marine Biomedical Research Institute of Qingdao (Qingdao, China). Female Balb/c nude mice (4−5 weeks) were purchased from the Beijing Vital River Laboratory Animal Technology Co., Ltd. HeLa cells (5×10^6 cells) were subcutaneously injected into the right forelimb armpit of the mice, and the mice were raised at SPF environment. After the tumor volume reached 1200 mm^3, Hypnorm/Midazolam was used to anesthetize the mice, and the tumor was cut into similar-sized pieces (2−3 mm^3) in the DMEM cell culture medium. A catheter was used to implant similar-sized tumoroids subcutaneously into the right forearm axilla of female BALB/c nude mice.

ASSOCIATED CONTENT

Supporting Information

The Supporting Information is available free of charge at https://pubs.acs.org/doi/10.1021/acsnano.0c10844.

Additional experimental section: Chemicals and materials; equipment; synthesis of the Au cores, ACSPs, fTDN; characterization; Raman imaging in living cells; RT-PCR; serum sample preparation; calculation of enhancement factor; photothermal properties of ACSPs; *in vitro* ROS detection; consumption of GSH; cell culture; cytotoxicity assays; AO/EB staining; flow cytometric analysis; *in vivo* antitumor effcacy; *in vivo* photothermal imaging; and *in vivo* potential toxicity analysis. Figures: Illustration of the synthesis of ACSPs; EDS spectra, FT-IR and XPS spectra of ACSPs; degradation of ACSPs and ACSNs; FDTD simulation; fluorescence quenching ability of ACSPs; analysis of AFM imaging and electrophoresis analysis of fTDN; optimization of assay parameters; specificity and stability of the nanodevice; MTT analysis; fluorescence images; SERS spectrum of miR-21 in MCF-7 and MDA-MB-231 cells; photothermal performance of ACSPs *in vitro*; temperature rise and fall curve of ACSNs; investigation of the ROS products; cytotoxicity study of ACSPs with different treatment for HeLa and HEK293 cell; flow apoptosis assay; H&E stained images of main organs from tumor-bearing mice; and blood biochemistry analysis and blood routine analysis from healthy mice. Tables: Sequences of oligonucleotides used in this work; comparison of various sensing system for miR-21 assay; quantification of miR-21 in different tumor cell by ERS spectra and qRT-PCR; and photothermal conversion efficiencies of various nanomaterials (PDF)

AUTHOR INFORMATION

Corresponding Author

Xiaoru Zhang − *Key Laboratory of Optic-electric Sensing and Analytical Chemistry for Life Science, Ministry of Education, Shandong Key Laboratory of Biochemical Analysis, and College of Chemistry and Molecular Engineering, Qingdao University of Science and Technology, Qingdao 266042, P.R. China;* orcid.org/0000-0002-2251-3208; Email: zhangxr7407@126.com

Authors

Peng He − *Key Laboratory of Optic-electric Sensing and Analytical Chemistry for Life Science, Ministry of Education, Shandong Key Laboratory of Biochemical Analysis, and College of Chemistry and Molecular Engineering, Qingdao*

University of Science and Technology, Qingdao 266042, P.R. China

Wenhao Han − *Key Laboratory of Optic-electric Sensing and Analytical Chemistry for Life Science, Ministry of Education, Shandong Key Laboratory of Biochemical Analysis, and College of Chemistry and Molecular Engineering, Qingdao University of Science and Technology, Qingdao 266042, P.R. China*

Cheng Bi − *Key Laboratory of Optic-electric Sensing and Analytical Chemistry for Life Science, Ministry of Education, Shandong Key Laboratory of Biochemical Analysis, and College of Chemistry and Molecular Engineering, Qingdao University of Science and Technology, Qingdao 266042, P.R. China*

Weiling Song − *Key Laboratory of Optic-electric Sensing and Analytical Chemistry for Life Science, Ministry of Education, Shandong Key Laboratory of Biochemical Analysis, and College of Chemistry and Molecular Engineering, Qingdao University of Science and Technology, Qingdao 266042, P.R. China*

Shuyan Niu − *Key Laboratory of Optic-electric Sensing and Analytical Chemistry for Life Science, Ministry of Education, Shandong Key Laboratory of Biochemical Analysis, and College of Chemistry and Molecular Engineering, Qingdao University of Science and Technology, Qingdao 266042, P.R. China*

Hong Zhou − *Key Laboratory of Optic-electric Sensing and Analytical Chemistry for Life Science, Ministry of Education, Shandong Key Laboratory of Biochemical Analysis, and College of Chemistry and Molecular Engineering, Qingdao University of Science and Technology, Qingdao 266042, P.R. China;* orcid.org/0000-0002-9264-7148

Complete contact information is available at: https://pubs.acs.org/10.1021/acsnano.0c10844

Notes

The authors declare no competing financial interest.

ACKNOWLEDGMENTS

This work was supported by the National Natural Science Foundation of China (nos. 21775080, 21705086, and 21675074) and Open Projects Fund of Shandong Key Laboratory of Carbohydrate Chemistry and Glycobiology, Shandong University (no. 2019CCG07).

REFERENCES

(1) Zhao, J.; Wallace, M.; Melancon, M. P. Cancer Theranostics with Gold Nanoshells. *Nanomedicine* **2014**, *9*, 2041−2057.

(2) Yu, Z.; Ge, Y.; Sun, Q.; Pan, W.; Wan, X.; Li, N.; Tang, B. A Pre-Protective Strategy for Precise Tumor Targeting and Efficient Photodynamic Therapy with a Switchable DNA/ Upconversion Nanocomposite. *Chem. Sci.* **2018**, *9*, 3563−3569.

(3) Condeelis, J.; Segall, J. E. Intravital Imaging of Cell Movement in Tumours. *Nat. Rev. Cancer* **2003**, *3*, 921−930.

(4) Chen, B.; Xu, P.; Wang, J.; Zhang, C. The Role of miRNA in Polycystic Ovary Syndrome (PCOS). *Gene* **2019**, *706*, 91−96.

(5) Meng, D.; Ma, W.; Wu, X.; Xu, C.; Kuang, H. DNA-Driven Two-Layer Core-Satellite Gold Nanostructures for Ultrasensitive MicroRNA Detection in Living Cells. *Small* **2020**, *16*, 2000003−2000011.

(6) Liang, C. P.; Ma, P. Q.; Liu, H.; Guo, X.; Yin, B. C.; Ye, B. C. Rational Engineering of a Dynamic, Entropy-Driven DNA Nanomachine for Intracellular MicroRNA Imaging. *Angew. Chem., Int. Ed.* **2017**, *56*, 9077−9081.

(7) Zhang, Z.; Wang, Y.; Zhang, N.; Zhang, S. Self-Assembly of Nucleic Acid Molecular Aggregates Catalyzed by a Triple-Helix Probe for miRNA Detection and Single Cell Imaging. *Chem. Sci.* **2016**, *7*, 4184−4189.

(8) Lujambio, A.; Lowe, S. W. The Microcosmos of Cancer. *Nature* **2012**, *482*, 347−355.

(9) Shen, Y.; Wu, T.; Tian, Q.; Mao, Y.; Hu, J.; Luo, X.; Ye, Y.; Chen, H. Y.; Xu, J. J. Engineering of ATP-Powered Photosensitizer for Targeted Recycling Activatable Imaging of MicroRNA and Controllable Cascade Amplification Photodynamic Therapy. *Anal. Chem.* **2019**, *91*, 7879−7886.

(10) Zhang, H.; Gao, W.; Liu, Y.; Sun, Y.; Jiang, Y.; Zhang, S. Electrochemiluminescence-Microscopy for MicroRNA Imaging in Single Cancer Cell Combined with Chemotherapy-Photothermal Therapy. *Anal. Chem.* **2019**, *91*, 12581−12586.

(11) Wang, J.; Wang, D. X.; Ma, J. Y.; Wang, Y. X.; Kong, D. M. Three-Dimensional DNA Nanostructures to Improve the Hyperbranched Hybridization Chain Reaction. *Chem. Sci.* **2019**, *10*, 9758−9767.

(12) Li, B. X.; Liu, Y. J.; Liu, Y. X.; Tian, T. T.; Yang, B. B.; Huang, X. D.; Liu, J. W.; Liu, B. H. Construction of Dual-Color Probes with Target-Triggered Signal Amplification for *in Situ* Single-Molecule Imaging of MicroRNA. *ACS Nano* **2020**, *14*, 8116−8125.

(13) Li, J. F.; Huang, Y. F.; Ding, Y.; Yang, Z. L.; Li, S. B.; Zhou, X. S.; Fan, F. R.; Zhang, W.; Zhou, Z. Y.; Wu, D. Y.; Ren, B.; Wang, Z. L.; Tian, Z. Q. Shell-Isolated Nanoparticle-Enhanced Raman Spectroscopy. *Nature* **2010**, *464*, 392−395.

(14) He, P.; Zhang, Y.; Liu, L.; Qiao, W.; Zhang, S. Ultrasensitive SERS Detection of Lysozyme by a Target-Triggering Multiple Cycle Amplification Strategy Based on a Gold Substrate. *Chem. - Eur. J.* **2013**, *19*, 7452−7460.

(15) Pérez-Jiménez, A. I.; Lyu, D.; Lu, Z.; Liu, G.; Ren, B. Surface-Enhanced Raman Spectroscopy: Benefits, Trade-Offs and Future Developments. *Chem. Sci.* **2020**, *11*, 4563−4577.

(16) Liu, J.; Zheng, T.; Tian, Y. Functionalized h-BN Nanosheets as a Theranostic Platform for SERS Real-Time Monitoring of MicroRNA and Photodynamic Therapy. *Angew. Chem., Int. Ed.* **2019**, *58*, 7757−7761.

(17) Zeng, Y.; Ren, J. Q.; Shen, A. G.; Hu, J. M. Splicing Nanoparticles-Based "Click" SERS Could Aid Multiplex Liquid Biopsy and Accurate Cellular Imaging. *J. Am. Chem. Soc.* **2018**, *140*, 10649−10652.

(18) Kapara, A.; Brunton, V.; Graham, D.; Faulds, K. Investigation of Cellular Uptake Mechanism of Functionalised Gold Nanoparticles into Breast Cancer Using SERS. *Chem. Sci.* **2020**, *11*, 5819−5829.

(19) Zhang, C.; Cui, X.; Yang, J.; Shao, X.; Zhang, Y.; Liu, D. Stimulus-Responsive Surface-Enhanced Raman Scattering: A "Trojan Horse" Strategy for Precision Molecular Diagnosis of Cancer. *Chem. Sci.* **2020**, *11*, 6111−6120.

(20) Liu, J.; Qu, Y.; Zheng, T.; Tian, Y. A Dual-Mode Nanoprobe for Evaluation of the Autophagy Level Affected by Photothermal Therapy. *Chem. Commun.* **2019**, *55*, 9673−9676.

(21) Huang, X.; Song, J.; Yung, B. C.; Huang, X.; Xiong, Y.; Chen, X. Ratiometric Optical Nanoprobes Enable Accurate Molecular Detection and Imaging. *Chem. Soc. Rev.* **2018**, *47*, 2873−2920.

(22) Wu, Y.; Xiao, F.; Wu, Z.; Yu, R. Novel Aptasensor Platform Based on Ratiometric Surface-Enhanced Raman Spectroscopy. *Anal. Chem.* **2017**, *89*, 2852−2858.

(23) Shi, H.; Chen, N.; Su, Y.; Wang, H.; He, Y. Reusable Silicon-Based Surface-Enhanced Raman Scattering Ratiometric Aptasensor with High Sensitivity, Specificity, and Reproducibility. *Anal. Chem.* **2017**, *89*, 10279−10285.

(24) Ye, S.; Wu, Y.; Wan, F.; Li, Y. A Seesaw Ratiometric Probe for Dual-Spectrum Imaging and Detection of Telomerase Activity in Single Living Cells. *Chem. Commun.* **2019**, *55*, 9967−9970.

(25) Zhang, P.; Jiang, J.; Yuan, R.; Zhuo, Y.; Chai, Y. Highly Ordered and Field-Free 3D DNA Nanostructure: The Next Generation of DNA Nanomachine for Rapid Single-Step Sensing. *J. Am. Chem. Soc.* **2018**, *140*, 9361−9364.

(26) Douglas, S. M.; Bachelet, I.; Church, G. M. A Logic-Gated Nanorobot for Targeted Transport of Molecular Payloads. *Science* **2012**, *335*, 831−833.
(27) Cha, T. G.; Pan, J.; Chen, H.; Salgado, J.; Li, X.; Mao, C.; Choi, J. H. A Synthetic DNA Motor that Transports Nanoparticles along Carbon Nanotubes. *Nat. Nanotechnol.* **2014**, *9*, 39−43.
(28) Yang, L.; Meng, L.; Song, J.; Xiao, Y.; Wang, R.; Kang, H.; Han, D. Dynamic Colloidal Nanoparticle Assembly Triggered by Aptamer-Receptor Interactions on Live Cell Membranes. *Chem. Sci.* **2019**, *10*, 7466−7471.
(29) Zhao, L.; Sun, R.; He, P.; Zhang, X. Ultrasensitive Detection of Exosomes by Target-Triggered Three-Dimensional DNA Walking Machine and Exonuclease III-Assisted Electrochemical Ratiometric Biosensing. *Anal. Chem.* **2019**, *91*, 14773−14779.
(30) Ma, P. Q.; Liang, C. P.; Zhang, H. H.; Yin, B. C.; Ye, B. C. A Highly Integrated DNA Nanomachine Operating in Living Cells Powered by an Endogenous Stimulus. *Chem. Sci.* **2018**, *9*, 3299−3304.
(31) Tepper, J.; Krasna, M. J.; Niedzwiecki, D.; Hollis, D.; Reed, C. E.; Goldberg, R.; Kiel, K.; Willett, C.; Sugarbaker, D.; Mayer, R. Phase III Trial of Trimodality Therapy with Cisplatin, Fluorouracil, Radiotherapy, and Surgery Compared with Surgery Alone for Esophageal Cancer: CALGB 9781. *J. Clin. Oncol.* **2008**, *26*, 1086−1092.
(32) Liu, Y.; Zhen, W.; Wang, Y.; Liu, J.; Jin, L.; Zhang, T.; Zhang, S.; Zhao, Y.; Song, S.; Li, C.; Zhu, J.; Yang, Y.; Zhang, H. One-Dimensional Fe_2P Acts as a Fenton Agent in Response to NIR II Light and Ultrasound for Deep Tumor Synergetic Theranostics. *Angew. Chem., Int. Ed.* **2019**, *58*, 2407−2412.
(33) Wu, D.; Li, B. L.; Zhao, Q.; Liu, Q.; Wang, D.; He, B.; Wei, Z.; Leong, D. T.; Wang, G.; Qian, H. Assembling Defined DNA Nanostructure with Nitrogen-Enriched Carbon Dots for Theranostic Cancer Applications. *Small* **2020**, *16*, 1906975−1906982.
(34) Liu, Y.; Wu, J.; Jin, Y.; Zhen, W.; Wang, Y.; Liu, J.; Jin, L.; Zhang, S.; Zhao, Y.; Song, S.; Yang, Y.; Zhang, H. Copper(I) Phosphide Nanocrystals for *in Situ* Self-Generation Magnetic Resonance Imaging-Guided Photothermal-Enhanced Chemodynamic Synergetic Therapy Resisting Deep-Seated Tumor. *Adv. Funct. Mater.* **2019**, *29*, 1904678−1904685.
(35) Hu, X.; Li, F.; Xia, F.; Guo, X.; Wang, N.; Liang, L.; Yang, B.; Fan, K.; Yan, X.; Ling, D. Biodegradation-Mediated Enzymatic Activity-Tunable Molybdenum Oxide Nanourchins for Tumor-Specific Cascade Catalytic Therapy. *J. Am. Chem. Soc.* **2020**, *142*, 1636−1644.
(36) Wu, Y.; Guo, T.; Qiu, Y.; Lin, Y.; Yao, Y.; Lian, W.; Lin, L.; Song, J.; Yang, H. An Inorganic Prodrug, Tellurium Nanowires with Enhanced ROS Generation and GSH Depletion for Selective Cancer Therapy. *Chem. Sci.* **2019**, *10*, 7068−7075.
(37) Curcio, A.; Silva, A. K. A.; Cabana, S.; Espinosa, A.; Baptiste, B.; Menguy, N.; Wilhelm, C.; Abou-Hassan, A. Iron Oxide Nanoflowers @ CuS Hybrids for Cancer Tri-Therapy: Interplay of Photothermal Therapy, Magnetic Hyperthermia and Photodynamic Therapy. *Theranostics* **2019**, *9*, 1288−1302.
(38) Wang, S.; Riedinger, A.; Li, H.; Fu, C.; Liu, H.; Li, L.; Liu, T.; Tan, L.; Barthel, M. J.; Pugliese, G.; De Donato, F.; Scotto D'Abbusco, M.; Meng, X.; Manna, L.; Meng, H.; Pellegrino, T. Plasmonic Copper Sulfide Nanocrystals Exhibiting Near-Infrared Photothermal and Photodynamic Therapeutic Effects. *ACS Nano* **2015**, *9*, 1788−1800.
(39) Liu, Z.; Liu, X.; Du, Y.; Ren, J.; Qu, X. Using Plasmonic Copper Sulfide Nanocrystals as Smart Light-Driven Sterilants. *ACS Nano* **2015**, *9*, 10335−10346.
(40) Lu, Y.; Li, L.; Lin, Z.; Wang, L.; Lin, L.; Li, M.; Zhang, Y.; Yin, Q.; Li, Q.; Xia, H. A New Treatment Modality for Rheumatoid Arthritis: Combined Photothermal and Photodynamic Therapy Using $Cu_{7.2}S_4$ Nanoparticles. *Adv. Healthcare Mater.* **2018**, *7*, 1800013−1800023.
(41) Chen, H.; Shao, L.; Li, Q.; Wang, J. Gold Nanorods and Their Plasmonic Properties. *Chem. Soc. Rev.* **2013**, *42*, 2679−2724.
(42) Lv, Q.; Min, H.; Duan, D. B.; Fang, W.; Pan, G. M.; Shen, A. G.; Wang, Q. Q.; Nie, G.; Hu, J. M. Total Aqueous Synthesis of Au@$Cu_{2-x}S$ Core-Shell Nanoparticles for *in Vitro* and *in Vivo* SERS/PA Imaging-Guided Photothermal Cancer Therapy. *Adv. Healthcare Mater.* **2018**, *8*, 1801257−1801267.
(43) Dong, L.; Li, K.; Wen, D.; Lu, Y.; Du, K.; Zhang, M.; Gao, X.; Feng, J.; Zhang, H. A Highly Active (102) Surface-Induced Rapid Degradation of a CuS Nanotheranostic Platform for *in Situ* T1-Weighted Magnetic Resonance Imaging-Guided Synergistic Therapy. *Nanoscale* **2019**, *11*, 12853−12857.
(44) Ma, B.; Wang, S.; Liu, F.; Zhang, S.; Duan, J.; Li, Z.; Kong, Y.; Sang, Y.; Liu, H.; Bu, W.; Li, L. Self-Assembled Copper-Amino Acid Nanoparticles for *in Situ* Glutathione "AND" H_2O_2 Sequentially Triggered Chemodynamic Therapy. *J. Am. Chem. Soc.* **2019**, *141*, 849−857.
(45) Rae, T. D.; Schmidt, P. J.; Pufahl, R. A.; Culotta, V. C.; V, O.; Halloran, T. Undetectable Intracellular Free Copper: The Requirement of a Copper Chaperone for Superoxide Dismutase. *Science* **1999**, *284*, 805−807.
(46) Zhu, H.; Wang, Y.; Chen, C.; Ma, M.; Zeng, J.; Li, S.; Xia, Y.; Gao, M. Monodisperse Dual Plasmonic Au@$Cu_{2-x}E$ (E= S, Se) Core@Shell Supraparticles: Aqueous Fabrication, Multimodal Imaging, and Tumor Therapy at *in Vivo* Level. *ACS Nano* **2017**, *11*, 8273−8281.
(47) Dutta, S.; Ray, C.; Mallick, S.; Sarkar, S.; Sahoo, R.; Negishi, Y.; Pal, T. A Gel-Based Approach to Design Hierarchical CuS Decorated Reduced Graphene Oxide Nanosheets for Enhanced Peroxidase-Like Activity Leading to Colorimetric Detection of Dopamine. *J. Phys. Chem. C* **2015**, *119*, 23790−23800.
(48) Huang, X.; Deng, G.; Liao, L.; Zhang, W.; Guan, G.; Zhou, F.; Xiao, Z.; Zou, R.; Wang, Q.; Hu, J. $CuCo_2S_4$ Nanocrystals: A New Platform for Multimodal Imaging Guided Photothermal Therapy. *Nanoscale* **2017**, *9*, 2626−2632.
(49) Lynge, M. E.; van der Westen, R.; Postma, A.; Städler, B. Polydopamine-A Nature-Inspired Polymer Coating for Biomedical Science. *Nanoscale* **2011**, *3*, 4916−4928.
(50) Lee, H.; Dellatore, S. M.; Miller, W. M.; Messersmith, P. B. Mussel-Inspired Surface Chemistry for Multifunctional Coatings. *Science* **2007**, *318*, 426−429.
(51) Yao, Y.; Zhao, D.; Li, N.; Shen, F.; Machuki, J. O. a.; Yang, D.; Li, J.; Tang, D.; Yu, Y.; Tian, J.; Dong, H.; Gao, F. Multifunctional Fe_3O_4@Polydopamine@DNA-Fueled Molecular Machine for Magnetically Targeted Intracellular Zn^{2+} Imaging and Fluorescence/MRI Guided Photodynamic-Photothermal Therapy. *Anal. Chem.* **2019**, *91*, 7850−7857.
(52) Qiang, W.; Li, W.; Li, X.; Chen, X.; Xu, D. Bioinspired Polydopamine Nanospheres: A Superquencher for Fluorescence Sensing of Biomolecules. *Chem. Sci.* **2014**, *5*, 3018−3024.
(53) Choi, C. K. K.; Li, J.; Wei, K.; Xu, Y. J.; Ho, L. W. C.; Zhu, M.; To, K. K. W.; Choi, C. H. J.; Bian, L. A Gold@Polydopamine Core-Shell Nanoprobe for Long-Term Intracellular Detection of Micro-RNAs in Differentiating Stem Cells. *J. Am. Chem. Soc.* **2015**, *137*, 7337−7346.
(54) He, L.; Lu, D.-Q.; Liang, H.; Xie, S.; Luo, C.; Hu, M.; Xu, L.; Zhang, X.; Tan, W. Fluorescence Resonance Energy Transfer-Based DNA Tetrahedron Nanotweezer for Highly Reliable Detection of Tumor-Related mRNA in Living Cells. *ACS Nano* **2017**, *11*, 4060−4066.
(55) Ma, W.; Fu, P.; Sun, M.; Xu, L.; Kuang, H.; Xu, C. Dual Quantification of MicroRNAs and Telomerase in Living Cells. *J. Am. Chem. Soc.* **2017**, *139*, 11752−11759.
(56) Huang, D. J.; Huang, Z. M.; Xiao, H. Y.; Wu, Z. K.; Tang, L. J.; Jiang, J. H. Protein Scaffolded DNA Tetrads Enable Efficient Delivery and Ultrasensitive Imaging of miRNA through Crosslinking Hybridization Chain Reaction. *Chem. Sci.* **2018**, *9*, 4892−4897.
(57) Wen, S.; Su, Y.; Dai, C.; Jia, J.; Fan, G. C.; Jiang, L. P.; Song, R. B.; Zhu, J. J. Plasmon Coupling-Enhanced Raman Sensing Platform Integrated with Exonuclease-Assisted Target Recycling Amplification

https://doi.org/10.1021/acsnano.0c10844
ACS Nano 2021, 15, 6961−6976

for Ultrasensitive and Selective Detection of MicroRNA-21. *Anal. Chem.* **2019**, *91*, 12298−12306.
(58) Liu, Q.; Ge, Z.; Mao, X.; Zhou, G.; Zuo, X.; Shen, J.; Shi, J.; Li, J.; Wang, L.; Chen, X.; Fan, C. Valency-Controlled Framework Nucleic Acid Signal Amplifiers. *Angew. Chem., Int. Ed.* **2018**, *57*, 7131−7135.
(59) Zhao, X.; Xu, L.; Sun, M.; Ma, W.; Wu, X.; Kuang, H.; Wang, L.; Xu, C. Gold-Quantum Dot Core-Satellite Assemblies for Lighting up MicroRNA *in Vitro* and *in Vivo*. *Small* **2016**, *12*, 4662−4668.
(60) He, X.; Zeng, T.; Li, Z.; Wang, G.; Ma, N. Catalytic Molecular Imaging of MicroRNA in Living Cells by DNA-Programmed Nanoparticle Disassembly. *Angew. Chem., Int. Ed.* **2016**, *55*, 3073−3076.
(61) Mohammadzadeh, P.; Cohan, R. A.; Ghoreishi, S. M.; Bitarafan-Rajabi, A.; Ardestani, M. S. AS1411 Aptamer-Anionic Linear Globular Dendrimer G2-Iohexol Selective Nano-Theranostics. *Sci. Rep.* **2017**, *7*, 11832−11847.
(62) Cross, J. B.; Currier, R. P.; Torraco, D. J.; Vanderberg, L. A.; Wagner, G. L.; Gladen, P. D. Killing of *Bacillus* Spores by Aqueous Dissolved Oxygen, Ascorbic Acid, and Copper Ions. *Appl. Environ. Microbiol.* **2003**, *69*, 2245−2252.
(63) Huang, X.; Deng, G.; Han, Y.; Yang, G.; Zou, R.; Zhang, Z.; Sun, S.; Hu, J. Right Cu_2-xS@MnS Core-Shell Nanoparticles as a Photo/H_2O_2-Responsive Platform for Effective Cancer Theranostics. *Adv. Sci.* **2019**, *6*, 1901461−1901473.
(64) Cao, Y.; Meng, X.; Wang, D.; Zhang, K.; Dai, W.; Dong, H.; Zhang, X. Intelligent MnO_2/$Cu_{2-x}S$ for Multimode Imaging Diagnostic and Advanced Single-Laser Irradiated Photothermal/Photodynamic Therapy. *ACS Appl. Mater. Interfaces* **2018**, *10*, 17732−17741.
(65) Ju, E.; Dong, K.; Chen, Z.; Liu, Z.; Liu, C.; Huang, Y.; Wang, Z.; Pu, F.; Ren, J.; Qu, X. Copper(II)-Graphitic Carbon Nitride Triggered Synergy: Improved ROS Generation and Reduced Glutathione Levels for Enhanced Photodynamic Therapy. *Angew. Chem., Int. Ed.* **2016**, *55*, 11467−11471.
(66) Dong, S.; Xu, J.; Jia, T.; Xu, M.; Zhong, C.; Yang, G.; Li, J.; Yang, D.; He, F.; Gai, S.; Yang, P.; Lin, J. Upconversion-Mediated $ZnFe_2O_4$ Nanoplatform for NIR-Enhanced Chemodynamic and Photodynamic Therapy. *Chem. Sci.* **2019**, *10*, 4259−4271.

https://doi.org/10.1021/acsnano.0c10844
ACS Nano 2021, 15, 6961−6976